



**Quantifying the effects of engineered nanomaterials on
endothelial cell architecture and vascular barrier integrity
using a cell pair model**

Journal:	<i>Nanoscale</i>
Manuscript ID	NR-ART-06-2019-004981.R1
Article Type:	Paper
Date Submitted by the Author:	29-Aug-2019
Complete List of Authors:	<p>Eweje, Feyisayo; Harvard University, Disease Biophysics Group, Wyss Institute for Biologically Inspired Engineering, John A. Paulson School of Engineering and Applied Sciences</p> <p>Ardoña, Herdeline Ann; Harvard University, Disease Biophysics Group, Wyss Institute for Biologically Inspired Engineering, John A. Paulson School of Engineering and Applied Sciences</p> <p>Zimmerman, John; Harvard University, Disease Biophysics Group, Wyss Institute for Biologically Inspired Engineering, John A. Paulson School of Engineering and Applied Sciences</p> <p>O'Connor, Blakely; Harvard University, Disease Biophysics Group, Wyss Institute for Biologically Inspired Engineering, John A. Paulson School of Engineering and Applied Sciences</p> <p>Ahn, Seungkuk; Harvard University, Disease Biophysics Group, Wyss Institute for Biologically Inspired Engineering, John A. Paulson School of Engineering and Applied Sciences</p> <p>Grevesse, Thomas; Harvard University, Disease Biophysics Group, Wyss Institute for Biologically Inspired Engineering, John A. Paulson School of Engineering and Applied Sciences; Concordia University, Department of Biology</p> <p>Rivera, Karla; Harvard University, Disease Biophysics Group, Wyss Institute for Biologically Inspired Engineering, John A. Paulson School of Engineering and Applied Sciences</p> <p>Bitounis, Dimitrios; Harvard University T H Chan School of Public Health, Demokritou, Philip; Harvard University, School of Public Health</p> <p>Parker, Kevin Kit; Harvard University, Wyss Institute; Harvard University, School of Engineering and Applied Sciences</p>

1 **Quantifying the effects of engineered nanomaterials on endothelial cell architecture and**
2 **vascular barrier integrity using a cell pair model**

3
4 *Feyisayo Eweje[‡], Herdeline Ann M. Ardoña,[‡] John F. Zimmerman, Blakely B. O'Connor,*
5 *Seungkuk Ahn, Thomas Grevesse, Karla N. Rivera, Dimitrios Bitounis, Philip Demokritou*
6 *and Kevin Kit Parker**

7
8 F. Eweje, Dr. H. A. M. Ardoña, Dr. J. F. Zimmerman, B. B. O'Connor, S. Ahn, Dr. T.
9 Grevesse. K. N. Rivera, Prof. K. K. Parker

10 Disease Biophysics Group, Wyss Institute for Biologically Inspired Engineering,
11 John A. Paulson School of Engineering and Applied Sciences

12 Harvard University

13 Cambridge, MA 02138, USA

14 E-mail: kkparker@seas.harvard.edu

15
16 Dr. T. Grevesse

17 Present Address: Department of Biology

18 Concordia University

19 Montréal, QC H3G 1M8, Canada

20
21 Dr. D. Bitounis, Prof. P. Demokritou

22 Center for Nanotechnology and Nanotoxicology

23 Department of Environmental Health

24 T. H. Chan School of Public Health

25 Harvard University

26 Boston, MA 02115, USA

27
28 [‡]F.E. and H.A.M.A. contributed equally.

29
30 **Keywords:** nanotoxicology, micropatterning, engineered nanomaterials, vascular barrier,
31 endothelial cells

1 Abstract

2
3 Engineered nanomaterials (ENMs) are increasingly used in consumer products due to their
4 unique physicochemical properties, but the specific hazards they pose to the structural and
5 functional integrity of endothelial barriers remain elusive. When assessing the effects of ENMs
6 on vascular barrier function, endothelial cell monolayers are commonly used as *in vitro* models.
7 Monolayer models, however, do not offer a granular understanding of how the structure-
8 function relationship of endothelial cells and tissues are disrupted due to ENM exposure. To
9 address this issue, we developed a micropatterned endothelial cell pair model to quantitatively
10 evaluate the effects of 10 ENMs (8 metal/metal oxides and 2 organic ENMs) on multiple
11 cellular parameters and determine how these parameters correlate to changes in vascular barrier
12 function. This minimalistic approach showed concerted changes in endothelial cell
13 morphology, intercellular junction formation, and cytoskeletal organization due to ENM
14 exposure, which were then quantified and compared to unexposed pairs using a “similarity
15 scoring” method. Using the cell pair model, this study revealed dose-dependent changes in actin
16 organization and adherens junction formation following exposure to representative ENMs (Ag,
17 TiO₂ and cellulose nanocrystals), which exhibited trends that correlate with changes measured
18 using an endothelial monolayer permeability assay. Together, these results demonstrate that we
19 can quantitatively evaluate changes in endothelial architecture emergent from nucleo-
20 cytoskeletal network remodeling using micropatterned cell pairs. The endothelial pair model
21 therefore presents potential applicability as a standardized assay for systematically screening
22 ENMs and other test agents for their cellular-level structural effects on vascular barriers.

23

1 **Introduction**

2 The vascular endothelium is a selective biological barrier that regulates the exchange of
3 proteins, fluids, and solutes between the intravascular fluid and surrounding vascularized
4 tissues. When damaged due to inflammatory agents, pathogens, or tissue injury, vascular
5 endothelial tissues can become dysfunctional and potentiate unnecessary interstitial fluid
6 accumulation, impaired tissue perfusion, and plasma protein leakage via paracellular
7 pathways.¹ Together, these events induce pathophysiological processes that contribute to organ
8 dysfunction in many disease states—most notably sepsis and septic shock.² Engineered
9 nanomaterials (ENMs), though increasingly incorporated into a variety of consumer products
10 due to their unique physiochemical properties,³ have been reported to cause negative effects on
11 the barrier function of the vascular endothelium.⁴⁻⁶ Particularly, several ENMs were shown to
12 induce changes in endothelial cell morphology, intercellular junction formation, and
13 cytoskeletal protein organization with negative ramifications on endothelial barrier function.⁷⁻
14 ¹² In such studies, tissue monolayers are commonly used as *in vitro* endothelial models for
15 assessing the effects of ENMs on vascular barrier structure and function. Although changes in
16 cellular-level features could lend important mechanistic insights into ENM toxicities,
17 monolayer models are typically used for monitoring tissue-level function and are often not
18 amenable for systematically measuring alterations in cellular structure during nanomaterial
19 exposure. The indeterminate cell size, shape, and orientation within endothelial monolayers
20 make it difficult to quantitatively analyze how ENMs may impact sub-cellular structures,
21 especially at lower doses of exposure.

22 Since the emergence of soft lithography in biological applications,¹³⁻¹⁵ micropatterned
23 multicellular assemblies have been considered a promising alternative model for systematically
24 evaluating morphological changes of cells or tissues in response to a plethora of external
25 stimuli.^{16, 17} Substrates with micropatterned proteins control the geometry of cells with sub-
26 micron resolution and thus recapitulate important aspects of the *in vivo* microenvironment by

1 dictating limits on cell architecture, adhesion, and spreading reminiscent of those imposed by
2 the extracellular matrix (ECM) and neighboring cells in the body.^{16, 18, 19} Protein
3 micropatterning has also been used for generating isolated cell pairs (*i.e.*, two cells sharing one
4 edge) to study epithelial cell-cell adhesion, junction organization, and stability,²⁰⁻²² as well as
5 to investigate cardiomyocyte electrical and structural coupling,²³⁻²⁵ cellular self-organization,²⁶
6 and contact-mediated keratinocyte differentiation.²⁷ Cell pairs effectively serve as the smallest
7 functional repeating unit of a continuous tissue, which are useful for modeling junction-
8 dependent cell interactions that occur in physiological tissue barriers. The confinement of cell
9 pairs within specific protein micropatterns therefore presents a way to systematically evaluate
10 the effects of different nanoparticle test agents on barrier tissues at a more local spatial scale.

11 In this study, we hypothesize that micropatterned endothelial cell pairs with defined
12 geometries and junction orientation can serve as a reductionist model for revealing how certain
13 ENMs induce concerted changes amongst structural features of vascular endothelial cells.
14 Because ECM protein micropatterns drive a reproducible cell pair shape and arrangement, this
15 model enables a systematic and quantitative analysis of changes in cellular-level structural
16 parameters that can be used as indicators of degrading barrier function. Here, structural changes
17 in endothelial cell pairs were measured following exposure to 10 different ENMs commonly
18 used for commercial or research purposes (Au, Ag, TiO₂, ZnO, SiO₂, CuO, Fe₂O₃, Al₂O₃ and 2
19 nanocellulose forms). Adherens junction protein expression and intercellular gap formation,
20 which are commonly correlated to the degree of paracellular permeability across endothelial
21 cells, were among the parameters measured using the pair model. In an effort to further
22 investigate how the impact of various ENMs on tissue barrier function are reflected in the
23 overall cellular structure, we also evaluated key cell architectural features such as cell
24 morphology, cytoskeletal reorganization (*e.g.*, transition from predominantly cortical actin to
25 stress fiber formation, changes in focal adhesion distribution) and nuclear morphology.
26 Additionally, the cell pair model serves as a probe for understanding how such cellular features

1 change due to the perturbation of cell-cell and cell-ECM interactions upon exposure to ENMs.
2 The summative ENM-induced changes in these endothelial structural features were then
3 assessed for their correspondence to effects on cellular viability and tissue-level barrier function.
4 The analyses described here will focus on decreasing endothelial barrier function due to
5 structural integrity degradation (*i.e.*, increased permeability) rather than barrier blockage by
6 external agents. Overall, endothelial cell pairs are demonstrated here as a reductionist model
7 for: (*i*) quantifying the cellular level effects of selected ENMs on endothelial barriers; (*ii*)
8 identifying the doses at which those ENMs start to structurally impact the cells; and (*iii*)
9 establishing whether such structural changes in cells correlate to functional effects at the
10 endothelial tissue-level.

11

12 **Results and Discussion**

13 ***Formation of Endothelial Cell Pairs***

14 Cell pairs, or two cells with a shared junction, serve as the basic functional repeating
15 unit of a continuous tissue such as the vascular endothelium (Fig. 1a). Here, endothelial cell
16 pairs with defined morphologies were produced by seeding human umbilical vein endothelial
17 cells (HUVECs) on protein micropattern arrays on a 2D substrate. Fibronectin (FN) is among
18 the ECM components that facilitates the attachment of vascular endothelial cells to the
19 basement membrane and supports tension-mediated processes that lead to changes in cell shape
20 and proliferation.^{28, 29} FN islands were shaped as two adjacent hexagons with a single shared
21 edge (Fig. 1a-c); the hexagonal shape mimics the polygonal, cobblestone-like shape of
22 confluent endothelial cells which maximizes the number of adjacent cells under physiological
23 conditions.³⁰ The microcontact-printed FN islands on polydimethylsiloxane (PDMS)-coated
24 glass substrates were then seeded with HUVECs to form cell pairs confined in bihexagonal
25 patterns. The cell pairs that underwent structural analysis were screened based on the following
26 criteria: (*i*) the FN island underlying the pair had a bihexagonal shape without defects; (*ii*) the

1 island contained two cells as evidenced by the presence of two nuclei, where each cell was
2 confined to a single hexagon of the island; and (iii) the two cells were directly adjacent to one
3 another, with their cell-cell junction area being within 45° to 90° of the long axis of the cell
4 pair. Selecting for this specific orientation enables a systematic comparison of shape- and
5 orientation-dependent structural parameters that can be measured from the images of
6 immunostained cell pairs under different exposure conditions. Additionally, imposing these
7 criteria normalizes intercellular tension between selected cell pairs, as junction length and
8 strength may vary with junction orientation and are affected by cellular tension.^{31, 32} However,
9 it is worth noting that the pair model does not account for the effect of multiple adjacent cells
10 bordering one cell in the native endothelium; this is instead simplified as a one-neighbor/one-
11 shared barrier model to increase the throughput of the assay model.

12 To promote the formation of cell pairs in this arrangement, each hexagon of the FN
13 island had an area of $2500 \mu\text{m}^2$, in accordance with the island area used to isolate single
14 endothelial cells in previous studies.^{33, 34} In addition to the shape being biomimetic, a hexagonal
15 morphology was selected to impose a low aspect ratio to the cells, which minimizes any prior
16 increase in cell stiffness that can occur when endothelial cells are forced to conform to shapes
17 with higher aspect ratios.³⁵ All experiments were conducted in static culture conditions, such
18 that any observed changes following ENM exposure would be independent of the influence of
19 shear stress on endothelial cell morphology. Following a 72-h culture period without ENM
20 exposure (Fig. 1d), an average of $13.96 \pm 0.84\%$ of the FN islands on a coverslip contained cell
21 pairs confined in the specified orientation eligible for screening using our assay ($n = 55$ images,
22 5 fields of view from 11 substrates).

23

24 ***Intracellular Localization and Cytotoxic Effects of ENMs***

25 After a 48-h culture period, the cell pairs were exposed to ENM dispersions for an
26 additional 24 hours (except for the control, unexposed cell pairs). To demonstrate the broad

1 utility of this assay for screening multiple nanomaterials, HUVEC pairs were exposed to 10
2 different ENMs of varying sizes and composition. This library of ENMs includes metals (Au,
3 18 nm; citrate-capped Ag, 22 nm) and metal oxides (TiO₂, 29 nm; ZnO, 46 nm; SiO₂, 15 nm;
4 CuO, 50 nm; Fe₂O₃, 10 nm; Al₂O₃, 28 nm), as well as polymorphs of an organic nanomaterial—
5 nanocellulose (cellulose nanocrystals, CNC, 250 nm × 25 nm; cellulose nanofibrils, CNF, 50
6 nm). These ENMs are commonly used for commercial applications, and therefore are good
7 representative samples for developing a generalizable ENM toxicity screening platform.

8 To assess the dose-dependency of the ENM-induced effects on endothelial cell
9 architecture, three ENMs were selected from this library to represent different ENM types:
10 citrate-capped Ag nanoparticles (NPs), photocatalytic-grade TiO₂ NPs, and CNC as
11 representatives of metal, metal oxide and organic nanomaterials, respectively. In our previous
12 work, Ag and TiO₂ at 100 µg/mL were shown to have significant effects on the contractility of
13 cardiac tissues, providing further reasoning for screening these ENMs for their effects on
14 vascular barrier cells.³⁶ Currently, nanomaterial-induced damage has been attributed to either
15 1) oxidative stress due to reactive oxygen species (ROS) formation, or 2) disruption of cell-cell
16 junctions, in conjunction with actin cytoskeleton remodeling.^{11, 37-39} Surface chemistry and size
17 have a significant influence on the mechanism of action of permeability-inducing ENMs.⁴⁰
18 Metal oxides such as ZnO, CuO and Fe₂O₃ were previously reported to induce increases in
19 intracellular ROS levels resulting in endothelial barrier gap formation.^{7, 37} On the other hand,
20 TiO₂ and SiO₂ have been reported to physically interact with cell-cell junctions, resulting in
21 intercellular gaps or inducing a signaling cascade that increases endothelial permeability.^{11, 38,}
22 ⁴¹ Interactions of nanocellulose with endothelial cells are less studied than the other inorganic
23 nanoparticles reported here, but previous reports suggest that they do not have significant
24 cytotoxic effects on endothelial cells.⁴² Regardless of the mechanism, alterations in cellular
25 structure precede the disruption of endothelial barrier function. In the subsequent sections, such

1 cellular-level changes induced by the aforementioned test ENMs will be quantified using
2 micropatterned cell pairs.

3 Using darkfield imaging, representative ENMs internalized by cells and displaying
4 significant optical scattering (TiO_2 , Fe_2O_3 , SiO_2) were observed to have a high propensity for
5 localization in the perinuclear region (Fig. 2a), which is consistent with previous reports.⁴³⁻⁴⁶
6 Due to the size range of the metal and metal oxide particles studied (~15 nm to 50 nm), the
7 observed perinuclear localization is further rationalized by the inability of ENMs to translocate
8 across the nuclear membrane, which has pore sizes (~5.2 nm) that may not be large enough for
9 the ENMs studied herein.⁴⁷ The cytotoxic effects of the selected ENMs were then measured at
10 different exposure levels (10 to 100 $\mu\text{g}/\text{mL}$) within a 24 h duration, in order to observe any
11 dose-dependent trends for each ENM type. First, a colorimetric assay based on 3-(4,5-
12 dimethylthiazol-2-yl)-5-(3-carboxymethoxyphenyl)-2-(4-sulfophenyl)-2*H*-tetrazolium (MTS)
13 was used on unpatterned HUVECs to assess dose-dependent ENM cytotoxicity. The measured
14 absorption of MTS-treated culture media correlates to mitochondrial reductase activity, and
15 therefore to cellular viability. For most metal/metal oxide particles studied here, a dose-
16 dependent decrease in cellular viability was observed, the two exceptions being Fe_2O_3 and
17 Al_2O_3 (Fig. 2b). Though only Fe_2O_3 exposure at 100 $\mu\text{g}/\text{mL}$ caused a statistically significant
18 increase in absorption, the increase observed in HUVECs post- Fe_2O_3 and Al_2O_3 exposure
19 suggests an increase in metabolic stress similar to what has been previously reported for other
20 nanomaterials.⁴⁸ The increase in metabolic stress as Fe_2O_3 dose increases is also consistent with
21 a previous report which showed that Fe_2O_3 nanoparticles enhance endothelial permeability by
22 promoting ROS-induced microtubule remodeling.⁷ No significant decrease in cellular viability
23 was detected for both nanocellulose polymorphs.

24 In addition, all of the ENMs induced a significant increase in release of lactate
25 dehydrogenase (LDH, a necrotic marker) with respect to the unexposed case, except for Ag at
26 10 $\mu\text{g}/\text{mL}$ (ESI Fig. S1a-b). Most notable LDH increases were observed for Ag (100 $\mu\text{g}/\text{mL}$),

1 TiO₂ (50 and 100 µg/mL), ZnO (10 µg/mL) and CuO (10 µg/mL)—all of which are consistent
2 with the decreased mitochondrial reductase activity detected using the MTS assay. Increasing
3 LDH release trends were also measured for Fe₂O₃ and Al₂O₃, which are the ENMs that showed
4 increasing metabolic activity as the ENM dose increases. These data suggest that HUVECs
5 exposed to Fe₂O₃ or Al₂O₃ undergo increases in metabolic stress and cell death at higher ENM
6 dosages. In addition, the expression of Ki67 in HUVECs with and without ENM exposure was
7 measured to compare cellular proliferation across the exposure conditions (ESI Fig. S1c-d) and
8 to demonstrate that the two cell-limit per island is maintained throughout the 72-h experiment
9 as per our analysis population criteria (see Figure 1d for experimental timeline). An increase in
10 cell proliferation could increase the number of FN islands per field of view that contain more
11 than two cells, which do not meet our criteria for analysis. Among the library of ENMs tested,
12 no significant increase in Ki67 expression was measured except under TiO₂ (100 µg/mL), CuO
13 (10 µg/mL), and Al₂O₃ (10 µg/mL) exposure as compared to the unexposed control. These
14 ENMs also caused an increase in LDH release, which may imply the necrotic cells under these
15 exposure conditions have less contact inhibition, resulting in increased propensity to proliferate.
16 On the other hand, less Ki67-positive cells were observed at higher doses of Fe₂O₃ (50 and 100
17 µg/mL). These data suggest that the majority of ENMs studied here do not significantly
18 increase the propensity of HUVECs to proliferate over the course of the 24-hour ENM exposure
19 period, therefore validating that the integrity of cell count per FN island is maintained
20 throughout the assay.

21

22 *ENM-Induced Changes in Cellular Morphology*

23 Because cellular retraction correlates to increased barrier permeability and increased
24 isometric tension exerted by cytoskeletal actin networks, ENM-induced changes in HUVEC
25 pair cell morphology were measured under different exposure conditions.⁴⁹ Here,
26 morphological changes in the cell pairs were quantified from the ratio between the total area of

1 each cell pair and the underlying FN island. This evaluation is important for determining the
2 direct effect of ENMs on morphology and in altering the integrity of adhesion of endothelial
3 cells to basement membrane ECM proteins.⁵⁰ The cell pair-to-FN island area ratio (AR) was
4 measured through analyzing actin- and FN-stained cell pair images (Fig. 3a). The dose-
5 dependent effects of Ag, TiO₂ and CNC on cellular morphology were also quantified using our
6 cell pair model (ESI Fig. S2 and Fig. 3b). Among the library of ENMs tested, Au, TiO₂, ZnO
7 and Al₂O₃ induced a significant decrease in AR at 10 µg/mL (ESI Fig. S3), while Ag caused an
8 increase in this ratio. While a decrease in AR value may be attributed to the onset of decreased
9 cellular viability, either cellular retraction or expansion can occur due to cytoskeletal
10 rearrangement when ENMs accumulate within the perinuclear region of the cell. Due to the
11 dynamic nature of cell spreading or retraction, we account for temporal variability in cell
12 morphology by averaging at least 20 cell pairs from two separate biological replicates per
13 analysis.

14 In the case of TiO₂ and CNC, a decrease in AR was observed with increasing ENM
15 dosage (Fig. 3b). While the cell retraction with increasing TiO₂ dosage corresponds to the
16 observed decrease in cell viability (Fig. 2b), the change in AR values when exposed to CNCs
17 cannot be attributed to a decrease in cell viability. This observation is similar to the case of Au,
18 TiO₂, ZnO and Al₂O₃ at 10 µg/mL. ENM screening using the micropatterned pair models
19 therefore allows the detection of the onset of significant structural changes even at doses which
20 do not affect cellular viability, such as in the case of CNC exposure. Interestingly, exposure to
21 Ag NPs at 50 µg/mL induced a dramatic increase in AR value corresponding to cellular
22 expansion, but decreases again at 100 µg/mL when a significant number of cells begin to
23 undergo cell death. Therefore, these observed cellular behaviors caused by ENM exposure
24 cannot solely be attributed to effects on cellular viability, but may also be due to the activation
25 of GTPase-dependent pathways that lead to cytoskeletal reorganization.⁵¹ Due to these findings,
26 in which the cells failed to abide by the ECM protein adhesion and shape cues, ENM-induced

1 endothelial cytoskeletal remodeling was further investigated as a potential explanation for this
2 behavior.

3

4 ***Remodeling of Cytoskeletal Organization Due to ENM Exposure***

5 To study cytoskeletal remodeling due to ENM exposure, changes in the organization
6 and intracellular distribution of actin filaments were quantified. Actomyosin contraction
7 regulates the permeability of endothelial layers. Filamentous actin at the periphery of cells
8 (cortical actin) serves as an important supporting network in intercellular junction formation
9 and cell-ECM adhesion,⁵² while contractile stress fibers are distributed across the cell body and
10 develop in response to permeability-increasing agents.^{49, 53, 54} Particularly, it is well-supported
11 that stress fiber formation is induced during myosin light-chain kinase and RhoA-Rho kinase
12 pathway activation, which consequently disrupts the integrity of adherens junctions.⁴⁹
13 Considering that the cytoskeleton has a vital role in shaping cellular architecture and in
14 maintaining the barrier integrity of endothelial tissues, quantifying changes in actin
15 organization and stress fiber formation is an important probe for screening ENMs that can
16 compromise the barrier function of endothelial cells. Previously, it has been reported that
17 certain nanoparticles can lead to actin fiber reorganization, resulting in increased endothelial
18 layer permeability.⁹ Here, we hypothesize that ENM exposure may disrupt barrier function by
19 shifting the distribution of polymerized actin in endothelial cells from cortical rings to central
20 stress fibers.

21 Cell pair actin distribution maps were generated by compiling actin-stained images for
22 each exposure condition into average intensity composites (Fig. 4 and ESI Fig. S4-S5). The
23 radial actin distribution from the center of each FN hexagon composing the cell pair island (Fig.
24 4g and ESI Fig. S6-S10) was then quantified for each ENM type. Two additional control groups
25 were used as a point of comparison: cell pairs treated with (i) calpeptin, a Rho activating drug,
26 which increases stress fiber formation; and (ii) Y-27632, a ROCK inhibiting drug, which

1 disrupts cortical actin formation (ESI Fig. S7). Results show a significant increase in
2 fluorescence signal from actin staining in the central region (0 to 15.5 μm from the center of
3 each hexagon) and a decrease in the peripheral region (15.5 to 31 μm), following exposure to
4 most ENMs at 10 $\mu\text{g}/\text{mL}$, except for Au (Fig. 4g and ESI Fig. S9-S10). Additionally, a dose-
5 dependent increase in stress fiber formation was observed as the ENM dose increased for Ag,
6 TiO_2 and CNC (Fig. 4d-f). At the cell-cell junctions, actin intensity was also significantly
7 greater after exposure to different doses of Ag, TiO_2 and CNC (ESI Fig. S11). In the case of Ag
8 at 100 $\mu\text{g}/\text{mL}$, where the cell viability is considerably low, the highly localized central signal
9 that is non-filamentous in nature can be attributed to the depolymerization of actin during
10 cellular death. Nonetheless, in most cases, increasing the ENM concentration leads to an
11 observable transition from predominantly cortical actin to the formation stress fibers
12 reminiscent of faulty endothelial barriers.

13 The expression of vinculin, an important protein in focal adhesion complexes, was also
14 assessed in the ENM-exposed and unexposed HUVEC pairs (ESI Fig. S12). Mapping the
15 distribution of focal adhesion proteins such as vinculin offers insight into the impact of ENMs
16 on cellular tension, because focal adhesion complexes are force-generating and tension-bearing
17 structures.⁵⁵ Immunostained vinculin features that are filamentous or elongated in nature were
18 predominantly colocalized with actin fibers (ESI Fig. S12-S13). As expected, calpeptin-
19 exposed (Rho-activated) and Y-27632-exposed (ROCK-inhibited) pairs showed increased and
20 decreased formation respectively of these features in the cell periphery relative to unexposed
21 pairs (ESI Fig. S14). However, these elongated vinculin features indicative of focal adhesions
22 were less pronounced at the cell edges for Ag-exposed HUVEC pairs as compared to unexposed
23 pairs. In addition, decreased vinculin localization at the junction area is particularly notable in
24 cell pairs exposed to all doses of Ag.

25 To gain a more specific and quantitative understanding of vinculin expression in the cell
26 pairs (pre- and post-ENM exposure), we measured vinculin distribution within the pairs using

1 a modified version of the method used to analyze actin distribution. Because of non-specific
2 vinculin staining observed largely in the middle of the cells, we conducted this analysis on the
3 periphery of the outer half of each pair (ESI Fig. S15). The cell periphery for the distribution
4 analysis here covers $R = 15.5 \mu\text{m}$ to $26.9 \mu\text{m}$ (an inscribed circle), as opposed to $31 \mu\text{m}$ to
5 reduce the number of potentially null pixels profiled. In agreement with the observations made
6 based on the vinculin heat maps, calpeptin-exposed pairs showed increased peripheral vinculin,
7 while Ag and TiO_2 -exposed pairs showed decreased peripheral vinculin at all exposure levels.
8 Because actin-bound vinculin is associated with both cell-cell and cell-ECM adhesions,⁵⁶ the
9 reduction of peripheral vinculin expression could be a cellular response to maintain balance in
10 intracellular and paracellular tension during ENM exposure, which is consistent with previous
11 reports.^{9, 22, 57}

12 Interestingly, immunostaining against FN showed features reminiscent of the
13 distribution patterns observed in actin and vinculin across the cell pairs. These cellular artefacts,
14 which were not observed on FN patterns without cells (Fig. 5a), provide evidence of cells
15 adhering to the substrate at localized points (*i.e.*, via focal adhesion complexes). The appearance
16 of these artefacts is consistent with the known ability of endothelial cell to rearrange exogenous
17 fibronectin.³⁴ These features were then used as an indicator for the distribution of tension-
18 bearing structures within cell. In particular, the colocalization of vinculin-FN pixels from the
19 images of immunostained cell pairs was measured as a metric for cell-ECM adhesion and to
20 validate the observed changes in vinculin localization after ENM exposure (Fig. 5b-c). Using
21 vinculin-FN colocalization to quantify focal adhesion distribution also further mitigated the
22 effects of non-specific vinculin staining, thus providing a more specific metric than vinculin
23 pixel intensity alone.

24 To assess changes in distribution of tension-bearing features within cell pairs (*i.e.*,
25 localized at the edge or at the center), radial distribution profiles were generated for all vinculin-
26 FN colocalization images (ESI Fig. S16). Consistent with the vinculin distribution results,

1 peripheral vinculin-FN colocalized pixel intensity was significantly decreased in Ag- and TiO₂-
2 exposed pairs at all doses relative to the unexposed controls. Contrary to the vinculin-only
3 analysis, calpeptin induced a decrease in relative colocalized pixel intensity between exposed
4 and unexposed pairs. This inconsistency suggests that the results of these two methods of
5 analysis (distribution of vinculin-only vs. vinculin-FN colocalized pixels) may vary if pairs are
6 exposed to factors that induce marked increase in focal adhesion density such as calpeptin.
7 Though the differences between the pixel intensities in CNC-exposed and unexposed pairs were
8 statistically significant, no clearly observable trend in variation was observed.

9 At the highest Ag concentration (100 µg/mL) and for calpeptin-exposed samples, total
10 (non-region specific) % colocalization of vinculin and FN was significantly higher than in the
11 unexposed condition (ESI Fig. S17). The former may be attributable to cell protein
12 rearrangement following cell death, similar to the actin rearrangement shown in Figure 4d. The
13 latter is likely the result of increased focal adhesion formation in the Rho-activated pairs. CNC
14 exposure at 50 and 100 µg/mL was also associated with a significant increase in %
15 colocalization, which is likely a byproduct of increased stress fiber formation (see ESI Fig. S9)
16 and thereby increased focal adhesion formation, as would be the expected response in an
17 otherwise normal cell. No trend in vinculin-FN colocalization was observed with respect to
18 TiO₂ dosage. Altogether, we show how this micropatterning-based assay enables the
19 quantification of stress fiber formation and the distribution of vinculin expression—both of
20 which are factors that suggest changes in the organization of tension-bearing cytoskeletal
21 proteins in response to ENM exposure as an external stimulus.

22

23 ***Changes in Nuclear Morphology and Separation Post-ENM Exposure***

24 Remodeling of the cytoskeleton can influence nuclear morphology via direct linkages
25 between the nuclear lamina and cytoskeleton, which could in turn modify chromatin dynamics,
26 gene expression, as well as mechanical homeostasis.⁵⁸⁻⁶¹ Given that several of the ENMs tested

1 here induced changes in endothelial actin distribution and stress fiber formation, we next sought
2 to determine whether ENM exposure had any effect on nuclear morphology and internuclear
3 separation. Because the actin networks of two cells are mechanically tethered to one another
4 via actin-associated adherens junctions, and to their respective nuclear lamina via linker
5 proteins bridging the nuclear envelope,^{59, 60} we hypothesized that ENM-induced actin
6 remodeling could lead to changes in nuclear eccentricity. Previous work has demonstrated that
7 nuclear elongation can occur as the result of combined lateral compressive and longitudinal
8 elongation forces applied by stress fibers in endothelial cells.⁶² We therefore used the cell pair
9 model to systematically measure changes in nuclear eccentricity as a function of ENM dosage.
10 Additionally, the assay was used to test whether exposure to select ENMs leads to changes in
11 internuclear separation and nuclear morphology (Fig. 6a). We define internuclear separation as
12 the distance between the center of the nuclei of the two cells in the pair (Fig. 6b). Nuclear
13 eccentricity was measured by fitting nuclei to ellipses as previously described (Fig. 6c).⁶³

14 After exposing the cell pairs to each of the 10 ENMs at a low concentration (10 $\mu\text{g}/\text{mL}$),
15 only TiO_2 and SiO_2 NPs induced a significant increase in internuclear separation (ESI Fig.
16 S18a). A significant increase in internuclear separation was also observed after exposing the
17 pairs to Ag NPs at a high concentration (100 $\mu\text{g}/\text{mL}$, Fig. 6d). Because contractile actomyosin
18 fibers bind cell nuclei and adherens junctions via interactions with VE-cadherin/catenin protein
19 complexes,^{64, 65} it is possible that the contraction of these fibers following Ag NP exposure at
20 10 and 50 $\mu\text{g}/\text{mL}$ decreases internuclear separation, while non-filamentous actin aggregates
21 observed after exposure at 100 $\mu\text{g}/\text{mL}$ (Fig. 4d) do not create this effect. While CNC exposure
22 did not result in any significant changes in nuclear parameters, TiO_2 exposure resulted in a
23 dose-dependent decrease in internuclear separation distance following an initial increase at the
24 10 $\mu\text{g}/\text{mL}$ dosage (Fig. 6d). Given that more stress fibers formed with increasing TiO_2 exposure
25 (Fig. 4e), contraction of these fibers could draw the nuclei together and result in this downward
26 trend.

1 While most ENMs did not show any statistically significant changes in nuclear
2 eccentricity in comparison to unexposed samples, increased nuclear elongation was observed
3 after Ag NP exposure at 10 $\mu\text{g}/\text{mL}$ (Fig. 6e and ESI Fig. S18b). Contrary to what was expected
4 due to increased stress fiber formation, eccentricity of the cell pair nuclei trended downwards
5 with increasing Ag NP dosage following this initial increase. This effect may be because
6 increasing the dosage of Ag increased the rate of cell death, as well as the degradation rate of
7 the actin cytoskeleton which occurs during the final stages of this process.^{66, 67} This observation
8 is consistent with higher cytotoxicity and apoptotic activity following Ag exposure relative to
9 TiO_2 and CNC (Fig. 2b and ESI Fig. S1a), as well as the appearance of the previously mentioned
10 non-filamentous actin aggregates in the cell pairs exposed to Ag NPs at 50 and 100 $\mu\text{g}/\text{mL}$.
11 Although TiO_2 and CNCs induced nominal increases in nuclear eccentricity as the dosage level
12 increased from 10 to 100 $\mu\text{g}/\text{mL}$, the trends were not statistically significant. Together, these
13 results show that our micropatterned model offers a way to not only measure changes in nuclear
14 eccentricity, but also to systematically quantify the internuclear separation between paired cells.

15

16 *ENM Effects on the Formation of Adherens Junctions and Intercellular Gaps*

17 Lastly, the direct impact of ENMs on the formation of endothelial adherens junctions,
18 which have an important role in the control of paracellular transport, was investigated using the
19 cell pair model. Actin filaments are tightly linked to these junctions; therefore, an orchestrated
20 balance in tension within this network is required for proper tissue development and
21 homeostasis.⁶⁸ When quantifying ENM-induced changes in cell-cell junction features, our
22 HUVEC pair model presents the advantage of having cells constrained to a defined area and
23 orientation, resulting in cell-cell contacts being in approximately the same location and of the
24 same length in each pair. Considering that the formation of adherens junctions is the result of
25 calcium-dependent homophilic interactions between vascular endothelial (VE)-cadherins in
26 adjacent cells,^{69, 70} the fluorescence intensity of immunostained VE-cadherins was

1 systematically measured along the intercellular junction area of the cell pairs. To observe VE-
2 cadherin expression, the cell pairs were stained with an anti-VE-cadherin antibody which binds
3 VE-cadherin independent of its dimerization state. VE-cadherin junction area expression was
4 quantified by first creating a linear profile along the midline of the junction area for an analyzed
5 pair, and then calculating the mean intensity of the pixels along the length of this profile (Fig.
6 7a). The reported values were averaged from these measured mean intensities, then normalized
7 with respect to the unexposed cell pairs. Confocal imaging conditions were made consistent
8 across all samples.

9 A significant decrease in intercellular junctional VE-cadherin expression intensity was
10 observed following exposure to CNC at 10 $\mu\text{g}/\text{mL}$ (0.92 ± 0.02 vs. 1 ± 0.02 in unexposed
11 samples), but no significant decrease was measured for any of the other ENMs tested at this
12 dosage level (Fig. 7b and ESI Fig. S19a).⁷¹ When cell pairs were exposed to higher dosages of
13 Ag, TiO_2 , and CNC, a decreasing VE-cadherin junction expression intensity was measured as
14 the dose increased from at 10 to 100 $\mu\text{g}/\text{mL}$ (Fig. 7b). These results suggest that each of these
15 three nanomaterials have a negative and dose-dependent impact on the formation of endothelial
16 adherens junctions.

17 Given that a decrease in adherens junction formation diminishes the strength of cell-cell
18 interactions, we next asked whether ENM exposure results in any structural changes at the cell-
19 cell junctions, such as the formation of intercellular endothelial gaps. Formation of endothelial
20 gaps *in vivo* provide a pathway for protein, fluid, and inflammatory cell leakage into body
21 tissues, resulting in a pathophysiological imbalance in both fluid homeostasis and inflammatory
22 cell activity. Intercellular gap formation was measured by identifying regions of interest within
23 actin-stained images of cell pairs where separation between the edges of the two cells was
24 visible despite the possibility of cell-cell contact, thresholding the image, and measuring the
25 total area of the observed gaps (Fig. 7c). Mean intercellular gap area is defined as the total gap
26 area observed in all pairs analyzed divided by the number of pairs analyzed, as opposed to the

1 number of gaps observed. This accounts for the variation in frequency of gap occurrence per
2 pair. The sample size is reported as the number of pairs containing at least one gap with a
3 minimum area of $2 \mu\text{m}^2$, which was the average area of small gaps in the intercellular junctional
4 area that were visible in VE-cadherin-stained cell pair images regardless of ENM exposure. No
5 significant gap formation was observed following exposure to any of the ENMs at $10 \mu\text{g/mL}$
6 (ESI Fig. S19b). This result is consistent with the absence of changes in intercellular junctional
7 VE-cadherin expression intensity following exposure to all ENMs tested at this dosage level,
8 with the exception of CNC. Significant intercellular gap formation was observed following
9 exposure to Ag and TiO_2 NP at $100 \mu\text{g/mL}$, with the mean gap size induced by Ag NPs (37.93
10 $\pm 17.18 \mu\text{m}^2$) being nominally larger than that induced by TiO_2 NPs ($24.42 \pm 20.04 \mu\text{m}^2$) (Fig.
11 7d and ESI Fig. S20-S21).

12 The findings discussed above were consistent with a previous report, demonstrating that
13 TiO_2 reduces junctional VE-cadherin expression leading to intercellular gap formation and
14 increased endothelial permeability.¹¹ It was shown that TiO_2 NPs ($23.5 \mu\text{m}$ diameter) directly
15 bind to VE-cadherin in adherens junction, disrupting the VE-cadherin homodimer, which
16 induces the phosphorylation of VE-cadherin at two protein residues and leads to internalization
17 and degradation. Importantly, the gap formation and increased permeability were shown to be
18 size-dependent, as TiO_2 microparticles (680 nm diameter) did not induce these effects, while
19 both Ag NPs (20 nm diameter) and SiO_2 NPs (15 nm diameter) did. Given that the Ag and TiO_2
20 NPs tested here were similar in size (with diameters of 22 and 29 nm , respectively), it is possible
21 that both NPs exert their effects through this mechanism, as supported by the previously-
22 mentioned work¹¹ and other studies showing Ag-induced VE-cadherin internalization.^{72, 73}
23 Other permeability-increasing and inflammatory agents have also been shown to induce VE-
24 cadherin phosphorylation, internalization, and intercellular gap formation in endothelial cells.⁷⁴
25 ⁷⁵ However, in addition to differences in surface chemistry, the CNCs tested (250 nm) here are
26 larger than the Ag and TiO_2 NPs, making it unlikely that the reduction in junctional VE-

1 cadherin expression observed following CNC exposure is the result of the same direct binding
2 mechanism. Previous studies have shown that CNCs exerted no cytotoxic effects on endothelial
3 cells (consistent with our MTS assay results in Fig. 2b) and were not taken up by the cells.⁷⁶ In
4 this case, it is possible that some other form of interaction between the nanocrystals and the
5 extracellular domain of the VE-cadherin proteins results in the significant decrease of VE-
6 cadherin in the intercellular junctional area.

7 Many of the ENM-exposed pairs also showed the appearance of “discontinuous”
8 adherens junctions (ESI Fig. S22), or areas along the intercellular junction line where junctional
9 proteins like VE-cadherin are distributed in short, linear structures that are approximately
10 perpendicular to the cell border.⁶⁵ As opposed to being associated with cortical F-actin, such
11 junctions are localized at the ends of stress fibers. Discontinuous adherens junction are formed
12 by the structural transformation of existing adherens junctions via cortical actin remodeling.⁶⁴
13 Subsequently, the contraction of actomyosin fibers associated with discontinuous adherens
14 junctions has been shown to induce junction deformation and the generation of intercellular
15 gaps in endothelial tissues.^{65, 77} Multiple ENMs were shown to induce stress fiber formation in
16 the EC pairs. Other than stimulating VE-cadherin homodimer dissociation via direct binding
17 (as with Ag or TiO₂ NPs), ENM-induced stress fiber formation resulting in increased junctional
18 tension and deformation is another potential mechanism by which ENM exposure contributes
19 to both decreased VE-cadherin junction area expression intensity and intercellular gap
20 formation as shown here.

21

22

23 ***Correlating Assay Parameters to Tissue-Level Permeability***

24 To compare ENM-induced cell- and tissue-level effects, the previously measured effects
25 of ENMs on cellular structural features (Fig. 8, black traces) were correlated to their impact on
26 HUVEC monolayer permeability (Fig. 8, red traces). The ENM-induced changes measured

1 using the cell pair model and the endothelial monolayer permeability assay were also compared
2 to assess the similarity in the gathered data trends from each approach. Tissue-level
3 permeability measurements were acquired for HUVEC monolayers exposed under the same
4 ENM dose range as in the cell pair studies (ESI Fig. S23). For these measurements, HUVECs
5 were grown on a Transwell membrane insert until confluency, after which the apical layers of
6 these wells were subjected to Ag, TiO₂ and CNC exposure at 10, 50 and 100 µg/mL for 24
7 hours.

8 As expected, increasing endothelial monolayer permeability corresponded to decreasing
9 AR or progressing cellular retraction as the TiO₂ dose increased (Fig. 8a). The TiO₂ dose-
10 dependent increase in monolayer permeability also correlated to the increase in stress fiber
11 formation, as measured from the centralized actin expression (Fig. 8b). These observations were
12 consistent with the trends from the cytotoxicity data in Fig. 2, as well as with literature
13 precedents that report a correlation between increased cellular tension due to the formation and
14 contraction of stress fibers, to cell retraction and increased monolayer permeability.⁵² The
15 trends in the two junctional parameters quantified (decrease in VE-cadherin junctional area
16 expression and increase in intercellular gap formation) also corresponded to increased
17 monolayer permeability as the TiO₂ dosage was increased (Fig. 8c-d); with the most significant
18 changes occurring between TiO₂ dosages of 50 and 100 µg/mL in both parameters. The TiO₂-
19 exposed cell pairs also showed the highest correlation coefficients between the measured
20 parameters and tissue permeability. However, no clear dose-dependent trends were observed in
21 monolayer permeability following Ag NPs and CNC exposure despite the dose-dependent
22 decrease in cellular viability due to Ag shown in Fig. 2. In the case of exposure with Ag NPs,
23 the unusual decrease in permeability at 50 µg/mL can be explained by the measured increase in
24 AR (Fig. 8a) and expansion of actin network (Fig. 8b). The permeability increases again when
25 the cell viability significantly decreases at 100 µg/mL Ag exposure. Additionally, these data
26 show that CNC exposure at 10 to 100 µg/mL leads to dose-dependent changes in cellular

1 morphology, stress fiber formation, and VE-cadherin expression, but does not significantly
2 affect cellular viability or tissue-level permeability (Fig. 8). Using the cell pair approach, we
3 also assessed the structural impact of Fe₂O₃ (ESI Fig. S24), which was previously reported to
4 increase endothelial permeability by upregulating ROS production.⁷ Our measurements show a
5 strong inverse correlation ($r = -0.956$) between the the dose-dependent changes in cell area and
6 tissue permeability (ESI Fig. S24c). These results are consistent with the cellular shrinkage
7 caused by ROS formation, which eventually degrades endothelial barrier function. Taken
8 together, these results across multiple types of ENMs demonstrate how this cell pair assay
9 provides information on nanomaterial-induced changes in cellular architecture parameters that
10 are not accessible using traditional cytotoxicity tests or assays based on monolayer tissues.

11 Finally, a similarity index scoring method was used to define a “healthy” cell pair
12 phenotype based on the unexposed cells with completely formed adherens junctions. In
13 particular, this method enables the quantification of the extent to which a cell pair deviates from
14 the unexposed phenotype after ENM exposure for 24 hours. The index implements a modified
15 implementation of the Hellinger distance formula, which is used to quantify the similarity
16 between two probability distributions (see ESI for the full discussion of the mathematical
17 approach).⁷⁸ This index combines the metrics which we defined in the sections above to be
18 important in screening whether an ENM induces dysfunction to an endothelial cell pair. The
19 index score falls between 0 and 100, where a score of 0 indicates that the distributions are
20 completely different (*i.e.*, no match between the exposed and unexposed cell pairs for that
21 exposure condition), and a score of 100 indicates that the distributions are completely identical
22 (*i.e.* a complete match between the exposed and unexposed cell pairs for that exposure
23 condition). Despite the absence of dose-dependent trends for some individual parameters, the
24 combined scores for each Ag and TiO₂ exposure condition showed a dose-dependent decrease
25 that coincided with increasing monolayer permeability (Fig. 9). The observed collective trends
26 for Ag and TiO₂ support how structural features of cells change in a concerted manner and

1 contribute to barrier dysfunction. Our model deconstructs the structural features of endothelial
2 cell pairs into measurable parameters while the associated scoring method allows for
3 quantitative comparisons between the effects of different ENM exposure conditions.
4 Altogether, the scoring index implemented here enables quantitative comparisons of sample
5 conditions imposed upon the cell pairs—allowing for the summative analysis of the effects of
6 ENM exposure on endothelial cell morphology, ECM adhesion, actin distribution, and
7 intercellular junction protein expression.

8

9 **Conclusions**

10 In this study, the influence of select ENMs on multiple key features of endothelial cell
11 architecture and cell-cell junctions were quantified using a reductionist micropatterning assay.
12 All measurements were performed on geometrically-controlled cell pairs with a specific
13 orientation, which can be formed reproducibly by seeding HUVECs on bihexagonal
14 micropatterns of a cell adhesion protein such as fibronectin. From these micropatterned
15 endothelial cell pairs, changes in morphological features, nucleo-cytoskeletal organization and
16 adherens junction formation after ENM exposure were measured. This approach revealed the
17 connections between changes in multiple cellular features, as well as their correlation to
18 changes in tissue-level endothelial barrier permeability upon exposure to ENMs at different
19 doses. Using our assay, the extent to which the tested ENMs induce deviations from a healthy
20 HUVEC pair phenotype were quantified using a “similarity index”, which evaluates the overlap
21 in values from two distributions of experimental data. Particularly, Ag and TiO₂ nanoparticles
22 showed a dose-dependent decline in score, indicating increasing deviation from the unexposed
23 phenotype. In the case of TiO₂, a dose-dependent trend was observed in cellular feature
24 deviation, which also correlated to increasing tissue-level permeability. Overall, we have
25 developed a quantitative assay based on micropatterned cell pairs, which aims to provide a
26 clearer probe into changes in cellular-level features due to permeability-inducing agents such

1 as some of the ENMs studied here. Importantly, this assay paves the way to consequently
2 monitor changes in cell-cell interactions and cell-ECM adhesion during and after ENM
3 exposure, which is rarely the case in traditional *in vitro* models of endothelial tissues. Therefore,
4 this endothelial cell pair model and the associated assay can be useful towards standardizing
5 the screening methods for assessing the effect of drugs and toxicants on cells with barrier-like
6 function in physiological settings.

7

8 **Experimental Section**

9 *PDMS stamp fabrication:* PDMS stamps for microcontact printing were prepared as
10 previously described.²³ A photolithographic mask was designed in AutoCAD (Autodesk Inc.)
11 and ordered from Output City (Brandon, OR, USA). Each mask consists of an array of
12 bihexagonal islands with a single shared edge, each shape having a total area of 5000 μm^2
13 (hexagon edge length, 31 μm). This mask was imposed on top of a silicon wafer (Wafer World,
14 FL, USA) spin-coated with SU-8 2002 negative photoresist (MicroChem Corp., MA, USA),
15 which was then exposed to UV light to crosslink the pattern. Uncrosslinked regions were
16 dissolved by submerging the wafers in propylene glycol methyl ether acetate, followed by
17 isopropyl alcohol, and then dried. PDMS (Sylgard 184, Dow Corning, MI, USA) was poured
18 over the wafer and then degassed in a vacuum desiccator. After curing, the patterned PDMS
19 was peeled off the surface and cut to be used as stamps (ESI Fig. S25).

20 *Micropatterning fibronectin on PDMS substrates:* PDMS stamps were sonicated in a
21 70% EtOH bath for a minimum of 15 minutes and dried with compressed air under a sterile
22 hood. The stamps were coated with 50 $\mu\text{g}/\text{mL}$ fibronectin (Sigma-Aldrich, MO, USA) for a
23 minimum of 45 minutes prior to patterning. Prior to this step, PDMS-coated 18-mm diameter
24 circular glass coverslips were prepared by spin-coating with Sylgard 184 PDMS, which was
25 cured overnight in a 65°C oven, and then pre-treated in a UV-ozone cleaner (Jelight, CA, USA)
26 for surface activation right before stamping. After fibronectin incubation, the stamps were

1 gently dried with compressed air and placed onto the UVO-treated coverslips to transfer
2 fibronectin in the desired pattern. Following pattern transfer, the coverslips were immersed in
3 1% Pluronic F127 (Sigma, MO, USA) for a minimum of 5 minutes to block cell adhesion to
4 unpatterned areas, then rinsed three times with phosphate buffered saline (PBS). The patterned
5 coverslips were stored in PBS at 4°C until cell seeding.

6 *Endothelial cell culture:* Human umbilical vein endothelial cells (Lonza, HUVECs)
7 were used for all the *in vitro* studies discussed in this study. HUVEC culture was maintained
8 under sterile conditions, at 37° C and 5% CO₂, using Medium 200 (Gibco, MA, USA) with the
9 corresponding low serum endothelial growth supplement (Thermo Fisher Scientific, MA, USA).
10 This medium supplement contains fetal bovine serum (2% v/v), hydrocortisone (1 µg/ml),
11 human epidermal growth factor (10 ng/ml) basic fibroblast growth factor (3 ng/ml) and heparin
12 (10 µg/ml). All cells used were between passage four to eight, with media exchange after 24
13 hours of seeding and every 48 hours thereafter. The micropatterned coverslips, with ~3600 FN
14 islands/cm², were placed in a standard 12-well plate and seeded with HUVECs at a density of
15 ~5,300 cells/cm². The cells were allowed to adhere to the fibronectin pattern, and the medium
16 was supplemented with 2.5 µM 8-CPT-cAMP (Abcam, MA, USA) between 24 to 72 hours
17 after seeding to ensure complete adherens junction formation.

18 *ENM synthesis and characterization:* The ENMs used in our experiments were procured,
19 synthesized, and characterized by Engineered Nanomaterials Coordination Core (ERCC)—part
20 of Nanotechnology Health Implications Research (NHIR) Consortium at Harvard School of
21 Public Health. Detailed synthesis and characterization of the ENMs used in this study have been
22 described elsewhere: citrate capped-capped Au and Ag NPs have been presented by Konduru
23 et al.⁷⁹ and Ahn et al.,³⁶ respectively; SiO₂, Fe₂O₃, and Al₂O₃ ENMs have been presented by
24 Beltran-Huarac et al.⁸⁰; CNC and CNF have been presented by Pyrgiotakis et al.⁸¹. The
25 following ENMs were commercially available: TiO₂ were purchased by Acros Organics and
26 have been previously characterized by Ahn et al.³⁶; CuO and ZnO were purchased from Sigma

1 Aldrich and Meliorum Technologies, respectively. The characterization data for CuO and ZnO
2 are presented in ESI Fig. S26 and Tables S1-S2.

3 *ENM dispersion preparation:* The dispersion preparation and colloidal characterization
4 were conducted according to literature procedures.⁸²⁻⁸⁴ We used an ultrasonic processor/sonic
5 dismembrator (FB-505, Fisher Scientific, USA) calibrated according to a literature protocol,⁸⁵
6 which was found to deliver an acoustic power of 2.51 J/s. Each ENM stock solution was
7 prepared with DNase/RNase free distilled water (Invitrogen, MA, USA) at a concentration of
8 500 µg/ml. To determine the minimum amount of sonication time for fully dispersing TiO₂,
9 ZnO, SiO₂, CuO, Fe₂O₃ and Al₂O₃ in water, the critical delivered sonication energy (DSE_{cr})
10 was first calculated for each ENM type according to a literature procedure.⁸⁶ The DSE_{cr} of a
11 specific ENM is defined as the DSE (in J/mL) required to achieve a solution with the lowest
12 particle agglomeration state in DI H₂O. A 1 mL solution from the stock was used to measure
13 the hydrodynamic diameter (dH) using dynamic light scattering (DLS; Malvern Nanosizer,
14 Worcestershire, UK). The solution was sonicated for 1 min, vortexed for 10 s, and measured
15 again. The process was continued until the dH and polydispersity index (PDI) values were not
16 changing significantly (± 5%).

17 All stock suspensions for the 6 ENMs mentioned above were then prepared in water
18 according to their respective DSE_{cr} values. The DSE_{cr} for these ENMs are as follows: TiO₂=
19 380 J/mL; ZnO= 420 J/mL; SiO₂= 161 J/mL; CuO= 271 J/mL; Fe₂O₃= 320 J/mL; Al₂O₃= 388.5
20 J/mL. The working solutions (10 to 100 µg/mL) for these ENMs were prepared by diluting the
21 sonicated 500 µg/mL stock solutions with HUVEC culture medium. For Au and Ag NPs, the
22 supplied colloidal solutions were concentrated to 1200 µg/mL by using ultracentrifugation at
23 13,000 RPM for 20 min at 4°C, which was then re-dispersed in water, vortexed for 30 s, and
24 then diluted to the final working concentrations with HUVEC cell culture media. For the
25 nanocellulose polymorphs (CNC and CNF), a 1 mg/mL stock solution was first prepared in
26 water and then vortexed at a high speed for 30 s seconds to ensure dispersion. The nanocellulose

1 stock solutions were diluted with HUVEC cell culture media to the desired final concentrations.
2 The DLS profiles for the stock solutions in water and ENM dispersions in cell culture media,
3 except for CNC and CNF that have higher aspect ratios, are presented in the ESI Fig. S27.

4 *ENM exposure studies:* After 24 h in normal culture and 24 h with cAMP-supplemented
5 media, HUVEC pairs were treated with ENMs at varying concentrations for another 24 h (Fig.
6 1d). For HUVEC monolayers, ENM suspension on cAMP-supplemented culture media was
7 introduced to the apical side of the well for 24 h. All ENM exposure experiments with HUVEC
8 pairs and monolayers were performed three times. For the studies with ENM-induced
9 cytoskeletal reorganization, cell pairs treated with calpeptin (Rho activator I, Cytoskeleton,
10 Inc.; working concentration= 1 unit/ mL) and Y-27632 (ROCK inhibitor, EMD Millipore;
11 working concentration= 10 μ M) were used as additional control groups. Exposure time for both
12 drugs is 30 minutes as per the manufacturer's protocol to achieve maximum effect on actin
13 fibers.

14 *Permeability assay:* HUVECs were seeded at a density of $\sim 15,000$ cells/ cm^2 on
15 Transwell® polyester membrane cell culture inserts (6.5 mm, 0.4 μm pore size, 0.33 cm^2
16 surface area; Corning, NY, USA). Prior to seeding, each insert was coated with 50 $\mu\text{g}/\text{mL}$ of
17 fibronectin for at least an hour at room temperature. The cells were cultured for 48 hours to
18 allow for confluence prior to permeability measurements. We followed a previously-reported
19 protocol⁸⁷ for calculating the macromolecular permeability of two representative fluorophores,
20 Alexa Fluor 555 (400 Da; Invitrogen, MA, USA) and Oregon Green 488 (1.2 kDa; Thermo
21 Fisher Scientific, MA, USA), across the HUVEC monolayers after 24 h of exposure to ENMs.
22 Permeability measurements were also taken before exposure to ENMs to ensure that all
23 monolayers have statistically similar permeability measurements prior to ENM exposure.

24 *Cytotoxicity measurements:* To measure ENM-induced changes in cellular viability,
25 commercially-available assay kits were used for detecting the release of lactate dehydrogenase
26 (LDH; Promega, WI, USA) and mitochondrial reductase activity using 3-(4,5-dimethylthiazol-

1 2-yl)-5-(3-carboxymethoxyphenyl)-2-(4-sulfophenyl)-2H-tetrazolium (MTS; Abcam, MA,
2 USA). For these tests, unpatterned HUVECs were seeded on 96-well plates at a density of
3 $\sim 15,600$ cells/cm². For the LDH assay, cell culture media were collected from each sample in
4 triplicate and then incubated with the reagents from the LDH assay kit. The absorbance of the
5 resulting solution at 490 nm was recorded using a plate reader (Synergy HT; BioTek, NJ, USA).
6 Similarly, the MTS assay was executed according to manufacturer's protocol, whereby the
7 absorption of test solutions was also recorded at 490 nm. To establish the correct baseline per
8 reading, the background signal at 650 nm and from each ENM suspension on fresh culture
9 media at 490 nm were subtracted from the recorded absorbance values.

10 *Immunostaining:* Cells were fixed in 4 % paraformaldehyde (PFA) for 10 min, followed
11 by permeabilization with 0.05% Triton-X for another 15 min. Non-specific binding was
12 prevented by blocking with a 5% bovine serum albumin (BSA) solution in PBS for 1 h. After
13 these steps, the samples were incubated with primary antibodies against vinculin (1:500; Abcam,
14 MA, USA), VE-cadherin (1:500; Abcam, MA, USA), or fibronectin (1:500; Sigma, MO, USA)
15 for 2 h at room temperature, followed by incubation with the appropriate secondary antibodies
16 (against rabbit IgG (H+L) conjugated to Alexa Fluor 488 or mouse IgG conjugated to Alexa
17 Fluor 633; 1:200; Life Technologies, CA, USA) and Alexa Fluor 546 Phalloidin (1:200; Life
18 Technologies, CA, USA) for 1 h at room temperature. To stain for nuclei, samples were
19 incubated with 4',6-diamidino-2-phenylindole dihydrochloride (DAPI; Invitrogen, CA, USA)
20 solution with a working concentration of at least 300 nM for 5 minutes. The samples were
21 washed at least three times with 0.5% BSA solution in between steps. After the last staining
22 step, all samples were washed with PBS for at least three times and then mounted on a glass
23 slide with Prolong Gold anti-fade agent (Life Technologies, CA, USA).

24 *Cellular proliferation measurements:* Proliferation of HUVECs with or without ENM
25 treatment were assessed by immunostaining against a Ki67 antibody as the proliferation marker
26 (1:500, Thermo Fisher Scientific, MA, USA; against rabbit IgG (H+L) conjugated to Alexa

1 Fluor 488) and DAPI for counting the total number of cells. The standard immunostaining
2 protocol described above was followed. For this measurement, unpatterned cells were seeded
3 on 24-well plates at a density of $\sim 5,300$ cells/cm². The % of Ki67-positive cells per number of
4 DAPI-positive cells were calculated and averaged from two independent experiments with 3
5 wells per treatment condition (least 4 fields of view per well).

6 *Darkfield microscopy:* ENM localization was observed using the darkfield mode of an
7 integrated hyperspectral and Raman microscope (CytoViva, AL, USA/ Horiba, CA, USA). The
8 corresponding darkfield images were obtained using a halogen lamp with aluminum reflector
9 (Part L1090; International Light Technologies, MA, USA). All test samples with HUVEC pairs
10 were fixed with 4% paraformaldehyde prior to mounting onto a glass slide with PBS.

11 *Confocal microscopy and data analysis:* All immunofluorescence images were acquired
12 using a spinning disk confocal microscope (Olympus ix83, Andor spinning disk). Image
13 analysis was conducted using Fiji, a distribution of ImageJ focused on biological image
14 analysis.⁸⁸ Further details on image analysis, quantification of cell pair features and calculation
15 of similarity index can be found in the Supporting Information. Custom ImageJ macros used
16 for image analysis are available from the authors upon request. All data shown are mean \pm
17 standard error of the mean (SEM). Pearson product-moment correlation coefficient was
18 calculated between the cellular architecture measurements and tissue permeability values
19 reported in Figure 8. Statistical significance was determined using a two-tailed Student's *t*-test
20 ($*p < 0.05$, $**p < 0.005$, $\#p < 0.001$).

21

22 **Supporting Information**

23 Electronic Supplementary Information (ESI) available: See DOI: 10.1039/x0xx00000x

24

25 **Conflicts of Interest**

26 There are no conflicts to declare.

1 **Acknowledgements**

2 Research reported in this publication was supported by National Institute of
3 Environmental Health Sciences of the National Institutes of Health under Award Number (NIH
4 grant number U01ES027272) as part of the Nanotechnology Health Implications Research
5 (NHIR) Consortium. The content is solely the responsibility of the authors and does not
6 necessarily represent the official views of the National Institutes of Health. The engineered
7 nanomaterials used in the research presented in this publication have been procured or
8 synthesized and characterized by the Engineered Nanomaterials Resource and Coordination
9 Core (ERCC) at the Center for Nanotechnology and Nanotoxicology at Harvard School of
10 Public Health, part of the NIEHS/NHIR consortium. This work was partially supported by the
11 Wyss Institute for Biologically Inspired Engineering at Harvard University. Soft lithography
12 work and darkfield imaging were performed at the Harvard Center for Nanoscale Systems
13 (CNS), which is a member of the National Nanotechnology Infrastructure Network (NNIN)
14 under NSF Award No. 1541959. The micropatterning experiments were performed in part at
15 the Harvard MRSEC (Grant No. DMR-1420570). F. E. thanks the Amgen Foundation for a
16 summer fellowship support. H. A. M. A. would like to thank the American Chemical Society
17 for generous support through the Irving S. Sigal Postdoctoral Fellowship. J. F. Z. acknowledges
18 support from Harvard University and by the Organ Design and Engineering Postdoctoral
19 Training (ODET) program through Brigham and Women's Hospital, National Institute of
20 Biomedical Imaging and Bioengineering (NIBIB) and the National Institute of Health (Award
21 No. 5-T32-EB016652-04). B.B.O. acknowledges support from the NIH Eunice Kennedy
22 Shriver National Institute of Child Health and Human Development (Award No. F31-
23 HD095594). The authors thank to Dr. Sean P. Sheehy for providing the software used for
24 similarity index measurements and Michael Rosnach for graphical assistance.

25

26

1 **References**

- 2 1. D. N. Granger and E. Senchenkova, in *Inflammation and the Microcirculation*,
3 Morgan & Claypool Life Sciences, San Rafael (CA), 2010, ch. Chapter 10,
4 Endothelial Barrier Dysfunction.
- 5 2. S. M. Opal and T. Poll, *Journal of Internal Medicine*, 2014, **277**, 277-293.
- 6 3. M. E. Vance, T. Kuiken, E. P. Vejerano, S. P. McGinnis, M. F. Hochella, Jr., D.
7 Rejeski and M. S. Hull, *Beilstein Journal of Nanotechnology*, 2015, **6**, 1769-1780.
- 8 4. Y. Cao, in *Cellular and Molecular Toxicology of Nanoparticles*, eds. Q. Saquib, M.
9 Faisal, A. A. Al-Khedhairy and A. A. Alatar, Springer International Publishing, Cham,
10 2018, DOI: 10.1007/978-3-319-72041-8_4, pp. 59-69.
- 11 5. J. D. Sisler, S. V. Pirela, S. Friend, M. Farcas, D. Schwegler-Berry, A. Shvedova, V.
12 Castranova, P. Demokritou and Y. Qian, *Nanotoxicology*, 2015, **9**, 769-779.
- 13 6. Y. Zhang and W. X. Yang, *Beilstein J Nanotechnol*, 2016, **7**, 675-684.
- 14 7. P. L. Apopa, Y. Qian, R. Shao, N. L. Guo, D. Schwegler-Berry, M. Pacurari, D.
15 Porter, X. Shi, V. Vallyathan, V. Castranova and D. C. Flynn, *Particle and Fibre*
16 *Toxicology*, 2009, **6**, 1.
- 17 8. K. Buyukhatipoglu and A. M. Clyne, *Journal of Biomedical Materials Research Part*
18 *A*, 2010, **96A**, 186-195.
- 19 9. Y. Liu, N. Rogel, K. Harada, L. Jarett, C. H. Maiorana, G. K. German, G. J. Mahler
20 and A. L. Doiron, *Nanotoxicology*, 2017, **11**, 846-856.
- 21 10. E. Paszek, J. Czyz, O. Woznicka, D. Jakubiak, J. Wojnarowicz, W. Lojkowski and E.
22 Stepien, *Journal of biomedical nanotechnology*, 2012, **8**, 957-967.
- 23 11. M. I. Setyawati, C. Y. Tay, S. L. Chia, S. L. Goh, W. Fang, M. J. Neo, H. C. Chong,
24 S. M. Tan, S. C. J. Loo, K. W. Ng, J. P. Xie, C. N. Ong, N. S. Tan and D. T. Leong,
25 *Nature Communications*, 2013, **4**, 1673.
- 26 12. C. Y. Tay, P. Cai, M. I. Setyawati, W. Fang, L. P. Tan, C. H. L. Hong, X. Chen and D.
27 T. Leong, *Nano Letters*, 2014, **14**, 83-88.
- 28 13. R. Singhvi, A. Kumar, G. P. Lopez, G. N. Stephanopoulos, D. I. C. Wang, G. M.
29 Whitesides and D. E. Ingber, *Science*, 1994, **264**, 696-698.
- 30 14. C. S. Chen, M. Mrksich, S. Huang, G. M. Whitesides and D. E. Ingber, *Science*, 1997,
31 **276**, 1425.
- 32 15. M. Mrksich and G. M. Whitesides, *Trends Biotechnol*, 1995, **13**, 228-235.
- 33 16. S. Alom Ruiz and C. S. Chen, *Soft Matter*, 2007, **3**, 168-177.

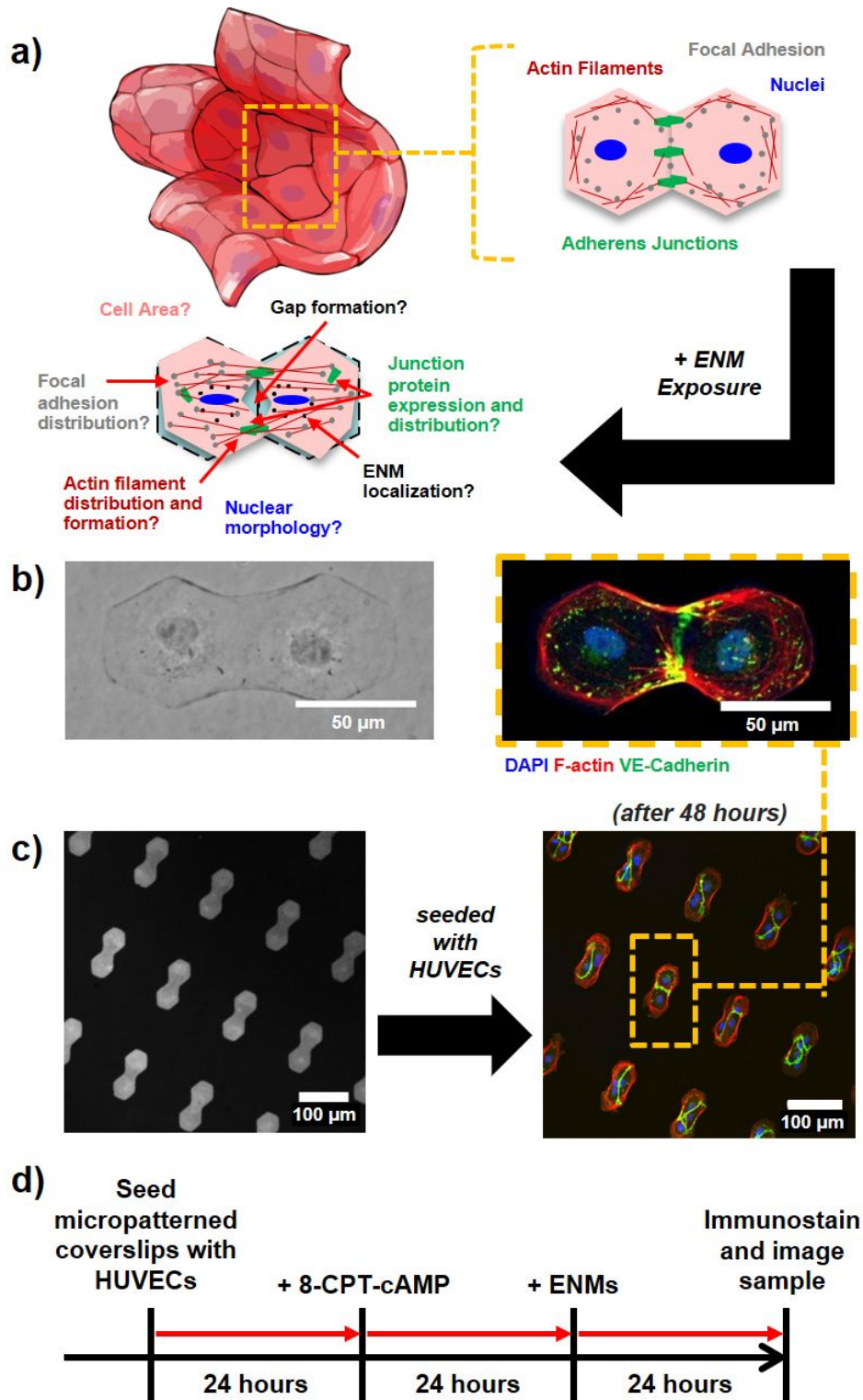
- 1 17. A. Quist, E. Pavlovic and S. Oscarsson, *Recent advances in microcontact printing*,
2 2005.
- 3 18. P. Leduc, E. Ostuni, G. Whitesides and D. Ingber, *Use of micropatterned adhesive*
4 *surfaces for control of cell behavior*, 2002.
- 5 19. N. F. Huang, E. S. Lai, A. J. Ribeiro, S. Pan, B. L. Pruitt, G. G. Fuller and J. P. Cooke,
6 *Biomaterials*, 2013, **34**, 2928-2937.
- 7 20. Q. Tseng, E. Duchemin-Pelletier, A. Deshiere, M. Balland, H. Guillou, O. Filhol and
8 M. Théry, *Proceedings of the National Academy of Sciences*, 2012, **109**, 1506.
- 9 21. B. Sarker, C. Walter and A. Pathak, *ACS Biomaterials Science & Engineering*, 2018,
10 **4**, 2340-2349.
- 11 22. J. Y. Sim, J. Moeller, K. C. Hart, D. Ramallo, V. Vogel, A. R. Dunn, W. J. Nelson and
12 B. L. Pruitt, *Mol Biol Cell*, 2015, **26**, 2456-2465.
- 13 23. M. L. McCain, T. Desplantez, N. A. Geisse, B. Rothen-Rutishauser, H. Oberer, K. K.
14 Parker and A. G. Kleber, *American Journal of Physiology - Heart and Circulatory*
15 *Physiology*, 2012, **302**, H443-H450.
- 16 24. L. C. McSpadden, H. Nguyen and N. Bursac, *Circulation. Arrhythmia and*
17 *electrophysiology*, 2012, **5**, 821-830.
- 18 25. D. M. Pedrotty, R. Y. Klinger, N. Badie, S. Hinds, A. Kardashian and N. Bursac, *Am J*
19 *Physiol Heart Circ Physiol*, 2008, **295**, H390-H400.
- 20 26. C. Brangwynne, K. K. Parker, S. Huang and D. E. Ingber, *In Vitro Cellular &*
21 *Developmental Biology - Animal*, 2000, **36**, 563-565.
- 22 27. J. L. Charest, J. M. Jennings, W. P. King, A. P. Kowalczyk and A. J. García, *Journal*
23 *of Investigative Dermatology*, 2009, **129**, 564-572.
- 24 28. D. E. Ingber, *Proc Natl Acad Sci U S A*, 1990, **87**, 3579-3583.
- 25 29. S. Huang and D. E. Ingber, *Nat Cell Biol*, 1999, **1**, E131-E138.
- 26 30. A. M. Malek and S. Izumo, *Journal of Cell Science*, 1996, **109**, 713.
- 27 31. Z. Liu, J. L. Tan, D. M. Cohen, M. T. Yang, N. J. Sniadecki, S. A. Ruiz, C. M. Nelson
28 and C. S. Chen, *Proceedings of the National Academy of Sciences*, 2010, **107**, 9944.
- 29 32. M. R. Ng, A. Besser, J. S. Brugge and G. Danuser, *eLife*, 2014, **3**, e03282.
- 30 33. C. S. Chen, M. Mrksich, S. Huang, G. M. Whitesides and D. E. Ingber, *Biotechnology*
31 *Progress*, 2008, **14**, 356-363.

- 1 34. K. K. Parker, A. L. Brock, C. Brangwynne, R. J. Mannix, N. Wang, E. Ostuni, N. A.
2 Geisse, J. C. Adams, G. M. Whitesides and D. E. Ingber, *The FASEB Journal*, 2002,
3 **16**, 1195-1204.
- 4 35. D. E. J. Anderson and M. T. Hinds, *Annals of Biomedical Engineering*, 2011, **39**,
5 2329.
- 6 36. S. Ahn, H. A. M. Ardoná, J. U. Lind, F. Eweje, S. L. Kim, G. M. Gonzalez, Q. Liu, J.
7 F. Zimmerman, G. Pyrgiotakis, Z. Zhang, J. Beltran-Huarac, P. Carpinone, B. M.
8 Moudgil, P. Demokritou and K. K. Parker, *Anal Bioanal Chem*, 2018, DOI:
9 10.1007/s00216-018-1106-7.
- 10 37. A. Nel, T. Xia, L. Madler and N. Li, *Science*, 2006, **311**, 622-627.
- 11 38. F. Peng, M. I. Setyawati, J. K. Tee, X. Ding, J. Wang, M. E. Nga, H. K. Ho and D. T.
12 Leong, *Nat Nanotechnol*, 2019, **14**, 279-286.
- 13 39. M. I. Setyawati, C. Y. Tay and D. T. Leong, *Nanomedicine*, 2014, **9**, 1591-1594.
- 14 40. A. E. Nel, L. Madler, D. Velegol, T. Xia, E. M. Hoek, P. Somasundaran, F. Klaessig,
15 V. Castranova and M. Thompson, *Nat Mater*, 2009, **8**, 543-557.
- 16 41. C. Y. Tay, M. I. Setyawati and D. T. Leong, *ACS Nano*, 2017, **11**, 2764-2772.
- 17 42. C. Endes, S. Camarero-Espinosa, S. Mueller, E. J. Foster, A. Petri-Fink, B. Rothen-
18 Rutishauser, C. Weder and M. J. Clift, *J Nanobiotechnology*, 2016, **14**, 78.
- 19 43. M. Liu, Q. Li, L. Liang, J. Li, K. Wang, J. Li, M. Lv, N. Chen, H. Song, J. Lee, J. Shi,
20 L. Wang, R. Lal and C. Fan, *Nat Commun*, 2017, **8**, 15646.
- 21 44. S. K. Lai, K. Hida, S. T. Man, C. Chen, C. Machamer, T. A. Schroer and J. Hanes,
22 *Biomaterials*, 2007, **28**, 2876-2884.
- 23 45. C. Dalal, A. Saha and N. R. Jana, *The Journal of Physical Chemistry C*, 2016, **120**,
24 6778-6786.
- 25 46. J. Zimmerman, H. A. M. Ardoña, G. Pyrgiotakis, J. Dong, B. M. Moudgil, P.
26 Demokritou and K. K. Parker, *Nano Letters*, 2019, DOI:
27 10.1021/acs.nanolett.8b03903.
- 28 47. D. Mohr, S. Frey, T. Fischer, T. Güttler and D. Görlich, *The EMBO Journal*, 2009, **28**,
29 2541.
- 30 48. J. F. Zimmerman, R. Parameswaran, G. Murray, Y. Wang, M. Burke and B. Tian,
31 *Science Advances*, 2016, **2**, e1601039.
- 32 49. S. Sukriti, M. Tauseef, P. Yazbeck and D. Mehta, *Pulm Circ*, 2014, **4**, 535-551.
- 33 50. G. E. Davis and D. R. Senger, *Circ Res*, 2005, **97**, 1093-1107.

- 1 51. N. Rogel, K. Harada, L. Jarett, C. H. Maiorana, G. K. German, G. J. Mahler and A. L.
2 Doiron, *Nanotoxicology*, 2017, **11**, 846-856.
- 3 52. N. Prasain and T. Stevens, *Microvasc Res*, 2009, **77**, 53-63.
- 4 53. Y. Komarova and A. B. Malik, *Annual Review of Physiology*, 2010, **72**, 463-493.
- 5 54. I. Singh, N. Knezevic, G. U. Ahmmed, V. Kini, A. B. Malik and D. Mehta, *J Biol*
6 *Chem*, 2007, **282**, 7833-7843.
- 7 55. K. Burridge and E. S. Wittchen, *The Journal of Cell Biology*, 2013, **200**, 9.
- 8 56. D. L. Huang, N. A. Bax, C. D. Buckley, W. I. Weis and A. R. Dunn, *Science*, 2017,
9 **357**, 703.
- 10 57. J. L. Bays and K. A. DeMali, *Cellular and Molecular Life Sciences*, 2017, **74**, 2999-
11 3009.
- 12 58. N. M. Ramdas and G. V. Shivashankar, *Journal of Molecular Biology*, 2015, **427**,
13 695-706.
- 14 59. D. A. Starr and H. N. Fridolfsson, *Annual Review of Cell and Developmental Biology*,
15 2010, **26**, 421-444.
- 16 60. A. J. Maniotis, C. S. Chen and D. E. Ingber, *Proceedings of the National Academy of*
17 *Sciences*, 1997, **94**, 849.
- 18 61. J.-K. Kim, A. Louhghalam, G. Lee, B. W. Schafer, D. Wirtz and D.-H. Kim, *Nature*
19 *Communications*, 2017, **8**, 2123.
- 20 62. M. Versaevel, T. Grevesse and S. Gabriele, *Nat Commun*, 2012, **3**, 671.
- 21 63. M.-A. P. Bray, W. J. Adams, N. A. Geisse, A. W. Feinberg, S. P. Sheehy and K. K.
22 Parker, *Biomaterials*, 2010, **31**, 5143-5150.
- 23 64. S. Huvneers, J. Oldenburg, E. Spanjaard, G. van der Krogt, I. Grigoriev, A.
24 Akhmanova, H. Rehmann and J. de Rooij, *The Journal of Cell Biology*, 2012, **196**,
25 641.
- 26 65. J. Millán, R. J. Cain, N. Reglero-Real, C. Bigarella, B. Marcos-Ramiro, L. Fernández-
27 Martín, I. Correas and A. J. Ridley, *BMC Biology*, 2010, **8**, 11.
- 28 66. M. Desouza, P. W. Gunning and J. R. Stehn, *BioArchitecture*, 2012, **2**, 75-87.
- 29 67. S. Povea-Cabello, M. Oropesa-Ávila, P. de la Cruz-Ojeda, M. Villanueva-Paz, M. de
30 la Mata, M. J. Suárez-Rivero, M. Álvarez-Córdoba, I. Villalón-García, D. Cotán, P.
31 Ybot-González and A. J. Sánchez-Alcázar, *International Journal of Molecular*
32 *Sciences*, 2017, **18**.

- 1 68. C. D. Buckley, J. Tan, K. L. Anderson, D. Hanein, N. Volkmann, W. I. Weis, W. J.
2 Nelson and A. R. Dunn, *Science*, 2014, **346**, 1254211.
- 3 69. M. Giannotta, M. Trani and E. Dejana, *Developmental Cell*, 2013, **26**, 441-454.
- 4 70. E. Dejana and F. Orsenigo, *Journal of Cell Science*, 2013, **126**, 2545.
- 5 71. M. Galisteo, M. Sánchez, R. o. Vera, M. González, A. Anguera, J. Duarte and A.
6 Zarzuelo, *The Journal of Nutrition*, 2005, **135**, 2399-2404.
- 7 72. H. Guo, J. Zhang, M. Boudreau, J. Meng, J.-j. Yin, J. Liu and H. Xu, *Particle and*
8 *Fibre Toxicology*, 2016, **13**, 21.
- 9 73. X. Sun, J. Shi, X. Zou, C. Wang, Y. Yang and H. Zhang, *Journal of Hazardous*
10 *Materials*, 2016, **317**, 570-578.
- 11 74. C. Cerutti and A. J. Ridley, *Experimental Cell Research*, 2017, **358**, 31-38.
- 12 75. A. P. Adam, *Mediators of Inflammation*, 2015, **2015**, 24.
- 13 76. S. Dong, A. A. Hirani, K. R. Colacino, Y. W. Lee and M. Roman, *Nano LIFE*, 2012,
14 **02**, 1241006.
- 15 77. D. Kugelmann, L. T. Rotkopf, M. Y. Radeva, A. Garcia-Ponce, E. Walter and J.
16 Waschke, *Scientific Reports*, 2018, **8**, 13229.
- 17 78. S. Ahn, H. A. M. Ardon, P. H. Campbell, G. M. Gonzalez and K. K. Parker, *ACS*
18 *Appl Mater Interfaces*, 2019, DOI: 10.1021/acsami.9b07626.
- 19 79. N. V. Konduru, R. M. Molina, A. Swami, F. Damiani, G. Pyrgiotakis, P. Lin, P.
20 Andreozzi, T. C. Donaghey, P. Demokritou, S. Krol, W. Kreyling and J. D. Brain,
21 *Part Fibre Toxicol*, 2017, **14**, 42.
- 22 80. J. Beltran-Huarac, Z. Zhang, G. Pyrgiotakis, G. DeLoid, N. Vaze, S. M. Hussain and
23 P. Demokritou, *NanoImpact*, 2018, **10**, 26-37.
- 24 81. G. Pyrgiotakis, W. Luu, Z. Zhang, N. Vaze, G. DeLoid, L. Rubio, W. A. C. Graham,
25 D. C. Bell, D. Bousfield and P. Demokritou, *Cellulose*, 2018, **25**, 2303-2319.
- 26 82. G. DeLoid, J. M. Cohen, T. Darrah, R. Derk, L. Rojanasakul, G. Pyrgiotakis, W.
27 Wohlleben and P. Demokritou, *Nature Communications*, 2014, **5**, 3514.
- 28 83. G. M. DeLoid, J. M. Cohen, G. Pyrgiotakis and P. Demokritou, *Nat Protoc*, 2017, **12**,
29 355-371.
- 30 84. G. M. DeLoid, J. M. Cohen, G. Pyrgiotakis, S. V. Pirela, A. Pal, J. Liu, J. Srebric and
31 P. Demokritou, *Part Fibre Toxicol*, 2015, **12**, 32.
- 32 85. J. S. Taurozzi, V. A. Hackley and M. R. Wiesner, *Nanotoxicology*, 2011, **5**, 711-729.

- 1 86. J. Cohen, G. Deloid, G. Pyrgiotakis and P. Demokritou, *Nanotoxicology*, 2013, **7**, 417-
2 431.
- 3 87. I. Bischoff, M. C. Hornburger, B. A. Mayer, A. Beyerle, J. Wegener and R. Fürst,
4 *Scientific Reports*, 2016, **6**, 23671.
- 5 88. J. Schindelin, I. Arganda-Carreras, E. Frise, V. Kaynig, M. Longair, T. Pietzsch, S.
6 Preibisch, C. Rueden, S. Saalfeld, B. Schmid, J.-Y. Tinevez, D. J. White, V.
7 Hartenstein, K. Eliceiri, P. Tomancak and A. Cardona, *Nature Methods*, 2012, **9**, 676.
- 8
- 9
- 10



1
2 **Figure 1. Formation of endothelial cell pairs on micropatterned substrates.** (a) Schematic
3 illustration of cell pairs as a functional repeating unit of the vascular endothelium and the local
4 structural parameters that can be assessed following ENM exposure. (b) Representative phase
5 contrast and confocal images of an endothelial cell pair. Healthy endothelial cell pairs formed
6 adherens junctions at the cell-cell contact border and expressed filamentous actin (F-actin)
7 around the cell cortex. (c) PDMS substrate patterned with double hexagon FN islands (area=
8 $2500 \mu\text{m}^2$ per hexagon) prior to endothelial cell seeding and 48 hours after seeding. (d)
9 Experimental timeline for endothelial cell pair ENM exposure studies.

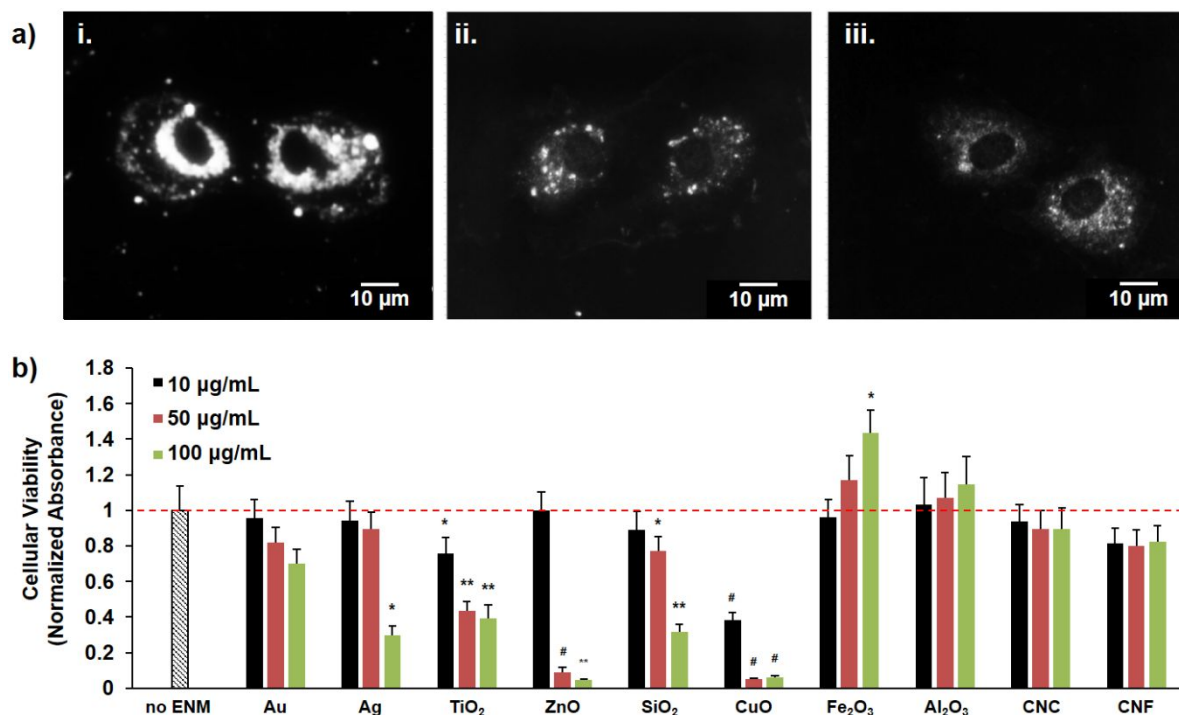
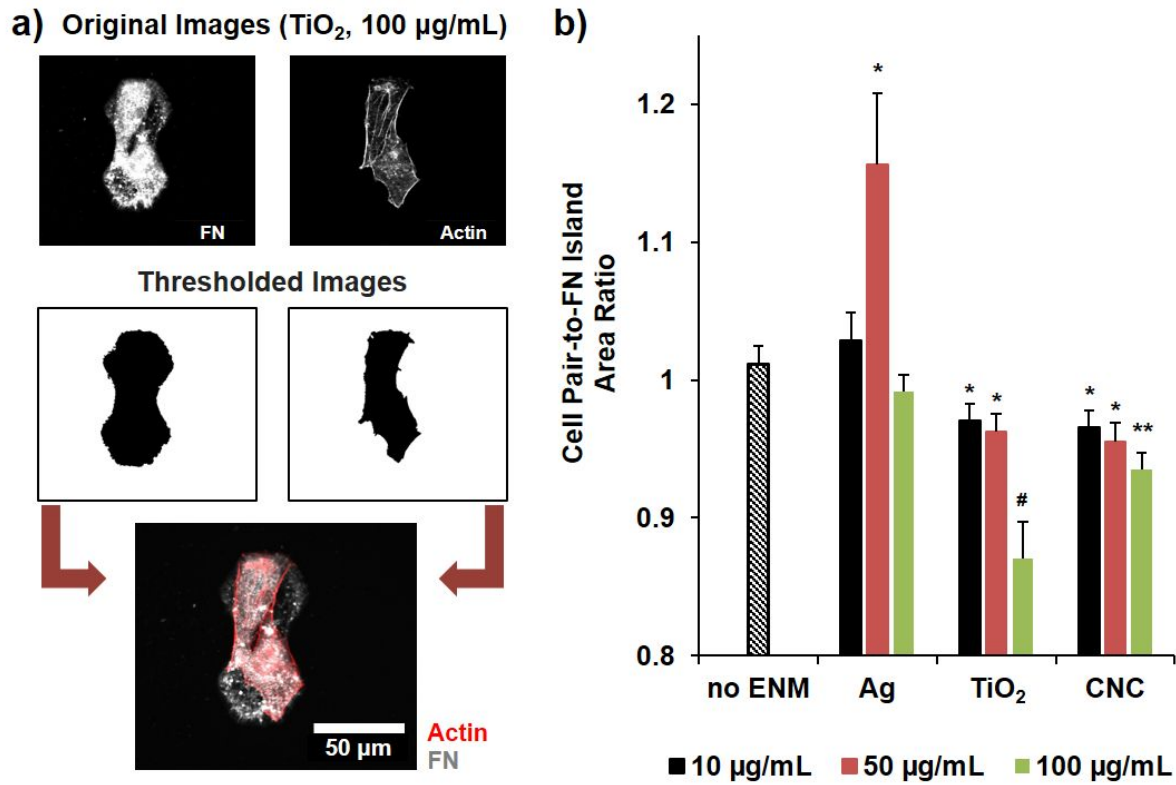


Figure 2. Distribution of ENMs in cell pairs following exposure and their cytotoxic effects.

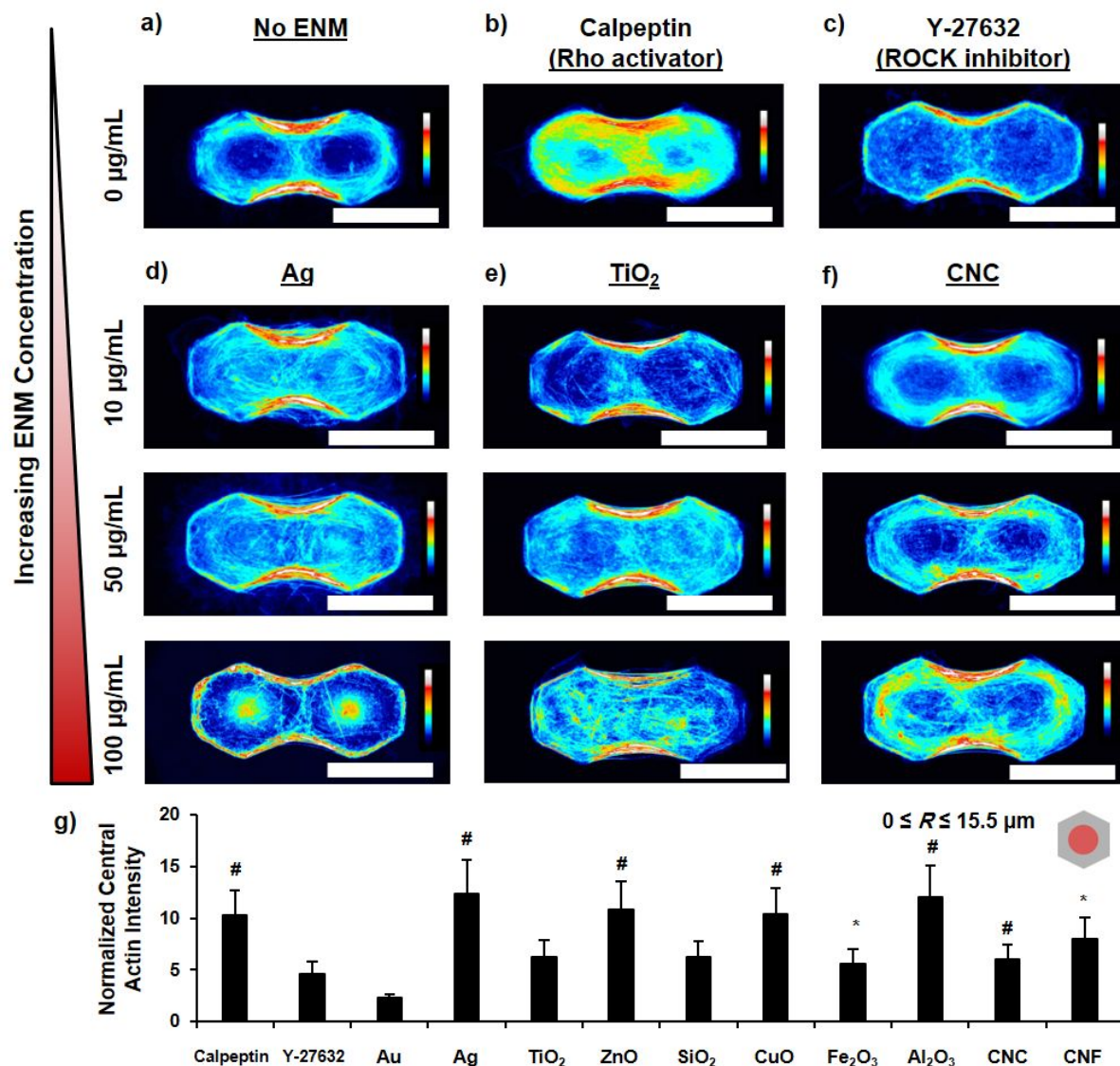
(a) Representative darkfield images of cell pairs exposed to 10 µg/mL of (i) TiO₂, (ii) Fe₂O₃ and (iii) SiO₂. (b) Cellular viability of unpatterned HUVECs after exposure to ENMs for 24 h, as determined by MTS assay; absorbance measurements normalized against the unexposed (no ENM) condition. Error bars represent standard error of mean; $n \geq 3$ per exposure condition, where n is the number of wells per exposure condition. Red dashed line represents the value for no ENM condition. For statistical comparison, * $p < 0.05$, ** $p < 0.005$, # $p < 0.001$ with respect to control.

1
2
3
4
5
6
7
8
9
10
11
12
13
14
15
16
17
18
19
20
21
22
23
24
25
26

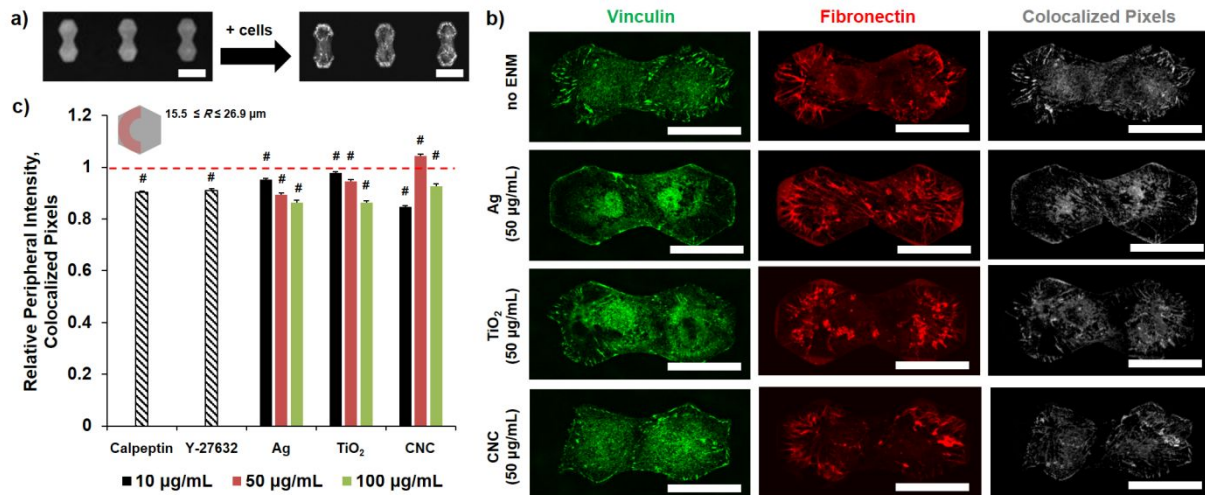


1
 2 **Figure 3. Impact of ENM exposure on the response of endothelial cells to extracellular**
 3 **shape cue.** (a) Schematic diagram of analysis method for calculating the cell pair-to-FN area
 4 ratio (AR). After thresholding FN and F-actin cell pair images, the cell pair area and fibronectin
 5 island area were measured, and the ratio was calculated. (b) AR values following exposure to
 6 Ag, TiO₂, and CNC at 10, 50, and 100 µg/mL ($n \geq 30$, where n is the number of cell pairs per
 7 exposure condition). For statistical comparison, * $p < 0.05$, ** $p < 0.005$, # $p < 0.001$ with respect
 8 to control.

9
 10
 11

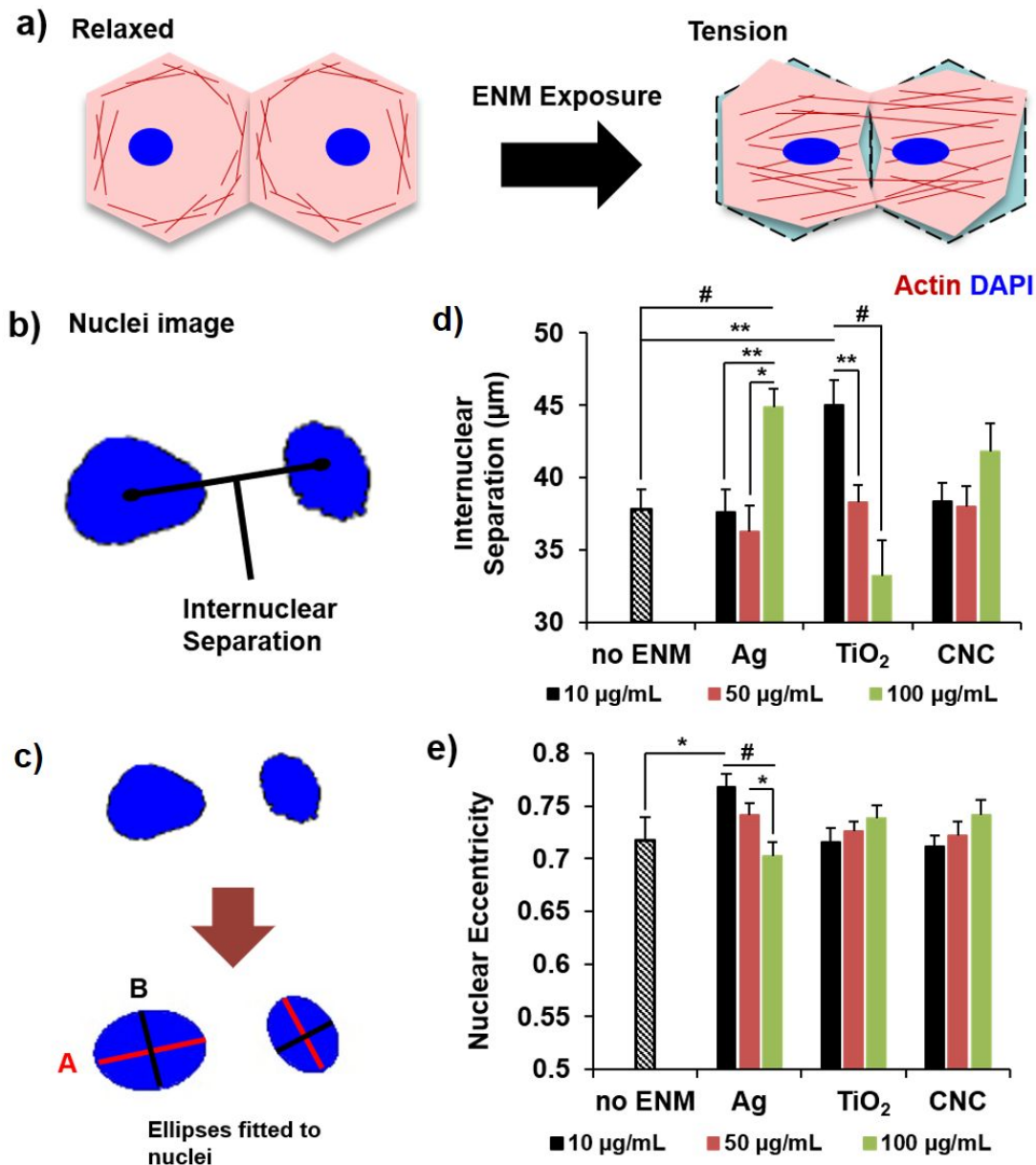


1
 2 **Figure 4. Dose-dependent effect of ENM exposure on actin filament distribution in**
 3 **endothelial cell pairs.** Composite confocal images of cell pairs immunostained against F-actin;
 4 (a) without ENM exposure, (b) with calpeptin (a Rho activating drug, induces stress fiber
 5 formation), (c) with Y-2763 (a ROCK inhibiting drug, disrupts cortical actin), and those
 6 exposed to 10 μg/mL, 50 μg/mL, and 100 μg/mL (d) Ag, (e) TiO₂ and (f) CNC for 24 hours.
 7 Scale bars= 50 μm; $n \geq 20$ per composite heat map, where n is the number of cell pairs per
 8 exposure condition. (g) Quantification of actin distribution in the central region (inset: red
 9 highlighted area, radius, R , = 0 to 15.5 μm from the center of a hexagonal cell)
 10 (10 μg/mL) patterned cells using radial scanning; normalized against the values for unexposed
 11 cell pairs (red dashed line). For statistical comparison, * $p < 0.05$, ** $p < 0.005$, # $p < 0.001$ with
 12 respect to control.
 13
 14
 15
 16
 17
 18
 19
 20



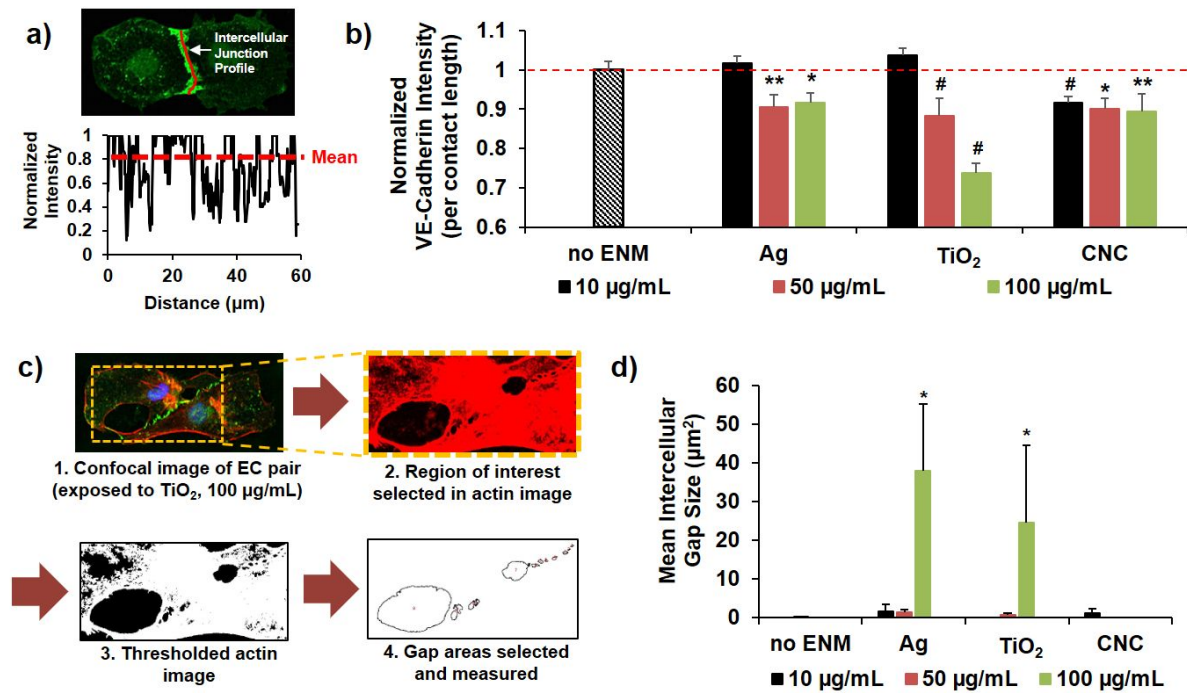
1
2 **Figure 5. Distribution of colocalized vinculin and fibronectin features.** (a) Micropatterned
3 bihexagonal FN island images (immunostained against FN) before and 72 h after cell seeding;
4 scale bars= 100 µm. (b) Representative images of cell pairs exposed to Ag, TiO₂ and CNC at 0
5 and 50 µg/mL, immunostained against vinculin and FN; scale bars=50 µm. Colocalization of
6 vinculin and FN pixels were defined using Costes method (see ESI). (c) Relative peripheral
7 intensity of colocalized vinculin and FN pixels (with respect to total vinculin pixels) for cell
8 pairs under different exposure conditions (inset: peripheral region pertains to the red highlighted
9 area, $R= 15.5$ to $26.9 \mu\text{m}$ of one cell). Red dashed line represents the measurement of unexposed
10 cell pairs (no ENM); $n \geq 10$, where n is the number of cell pairs per exposure condition.

11
12
13
14
15
16



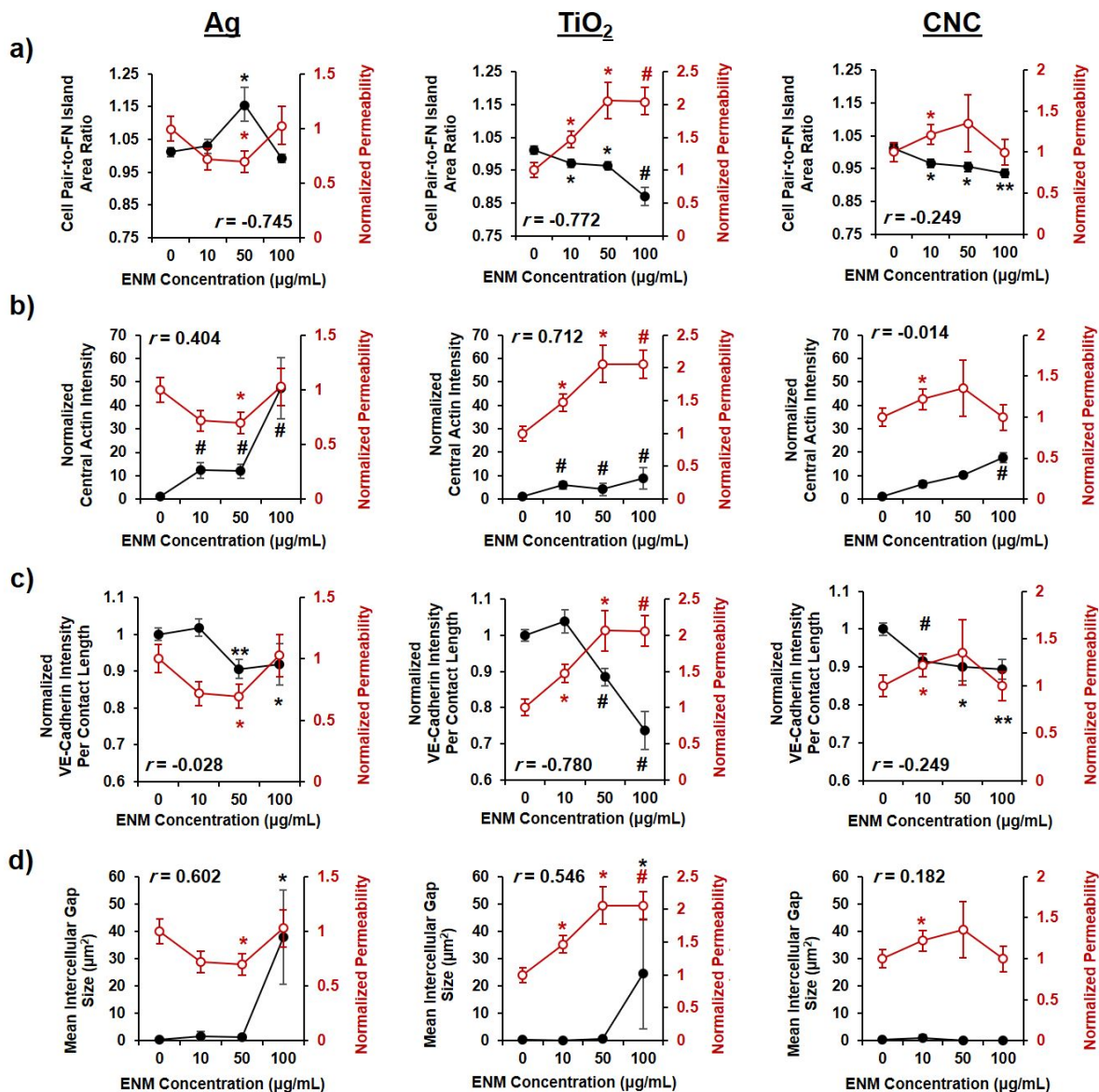
1
 2 **Figure 6. Dose-dependent effect of ENM exposure on distance between endothelial cell**
 3 **pair nuclei and nuclear eccentricity.** (a) Illustration of tension-induced nuclear remodeling of
 4 cell pairs following ENM exposure. (b) Schematic diagram depicting the analysis procedure
 5 used to determine cell pair internuclear separation. Internuclear separation was defined as the
 6 distance between the centers of the nuclei of the two cells. (c) Schematic diagram depicting
 7 nuclei fitted to ellipses for measuring nuclear eccentricity, resulting in values from 0 to 1, where
 8 0 corresponds to a circle. (d) Internuclear separation following exposure to Ag, TiO₂, and CNC
 9 at 10, 50, and 100 µg/mL ($n \geq 20$, where n is the number of cell pairs per exposure condition).
 10 (e) Nuclear eccentricity following exposure to Ag, TiO₂, and CNC at 10, 50, and 100 µg/mL (n
 11 ≥ 40 , where n is the total number of cells per exposure condition). For statistical comparison,
 12 $*p < 0.05$, $**p < 0.005$, $\#p < 0.001$.

13
 14



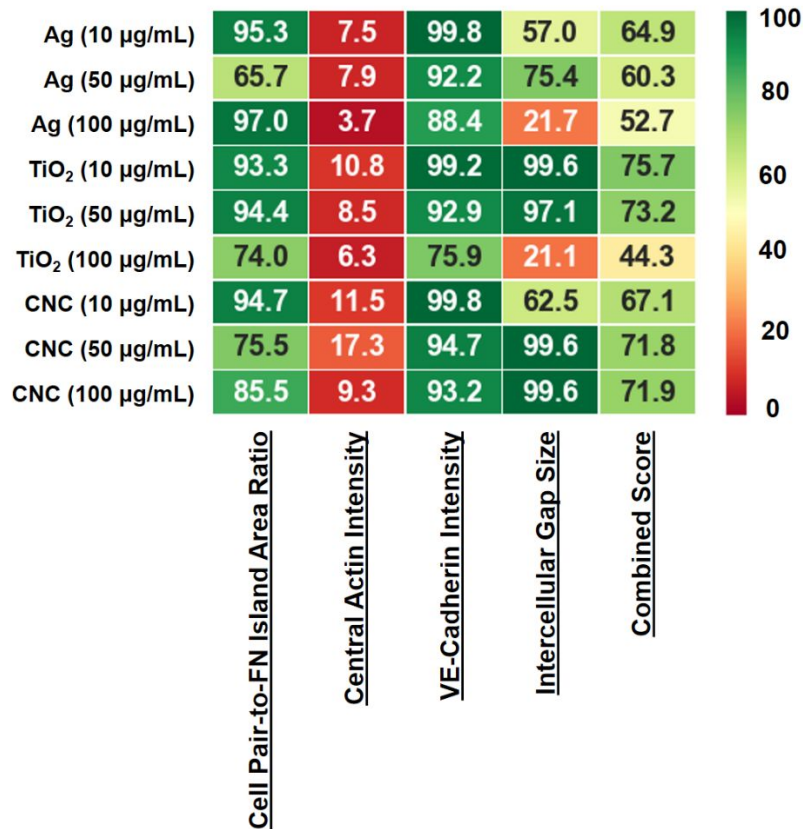
1
2
3 **Figure 7. Changes in VE-cadherin expression and formation of intercellular gaps between**
4 **endothelial cell pairs due to ENM exposure.** (a) Procedure for measuring VE-cadherin
5 expression intensity per contact length in the intercellular junction area. A linear profile was
6 created along the midline of the junction area for each analyzed pair and the mean intensity of
7 the pixels composing the profile was calculated. The values reported are an average of these
8 measured mean intensities, normalized with respect to the unexposed cell pairs. (b) VE-
9 cadherin intensity per contact length following exposure to Ag, TiO₂, and CNC at 10, 50, and
10 100 $\mu\text{g}/\text{mL}$ ($n \geq 20$, where n is the number of cell pairs per exposure condition). Red dashed
11 line represents the value for no ENM condition. (c) Procedure for measuring intercellular gap
12 size in EC pairs. d) Mean intercellular gap size following exposure to Ag, TiO₂, and CNC at
13 10, 50, and 100 $\mu\text{g}/\text{mL}$ ($n \geq 20$, where n is the number of cell pairs per exposure condition). For
14 statistical comparison, * $p < 0.05$, ** $p < 0.005$, # $p < 0.001$ with respect to control.

15
16
17
18
19
20
21
22



1
2
3 **Figure 8. Correlation plots: changes in cellular architecture correlated to endothelial**
4 **barrier permeability.** (a) Cell pair-to-FN island area ratio or AR, (b) central actin intensity
5 ratio, (c) VE-cadherin expression intensity in intercellular junction area, and (d) mean
6 intercellular gap size (all black) plotted with EC monolayer permeability (red, normalized with
7 respect to unexposed conditions) as a function of ENM exposure level. For statistical
8 comparison, * $p < 0.05$, ** $p < 0.005$, # $p < 0.001$ with respect to control. The correlation
9 coefficient, r , between a cellular architecture parameter and tissue permeability is reported in
10 each plot.

11
12
13
14
15
16
17



1
2
3 **Figure 9. Similarity index based on cell pair assay metrics.** Cell pair scoring index, which
4 compares the state of cell pairs exposed to different ENM conditions and those that are
5 “healthy”, unexposed endothelial cell pairs. The index is a modified implementation of the
6 Hellinger distance formula, which is used to quantify the similarity between two probability
7 distributions. A score of 100 indicates complete similarity between two data sets, while a score
8 of 0 indicates complete dissimilarity. The combined score represents the average score from
9 the following individual parameters: cell pair-to-FN island area ratio, central actin intensity,
10 VE-cadherin intensity, and intercellular gap size.

11
12
13
14
15
16
17
18
19
20
21
22
23
24
25
26
27
28
29

1 **TABLE OF CONTENTS ENTRY:**

2

3 **Quantifying the effects of engineered nanomaterials on endothelial cell architecture and**
4 **vascular barrier integrity using a cell pair model**

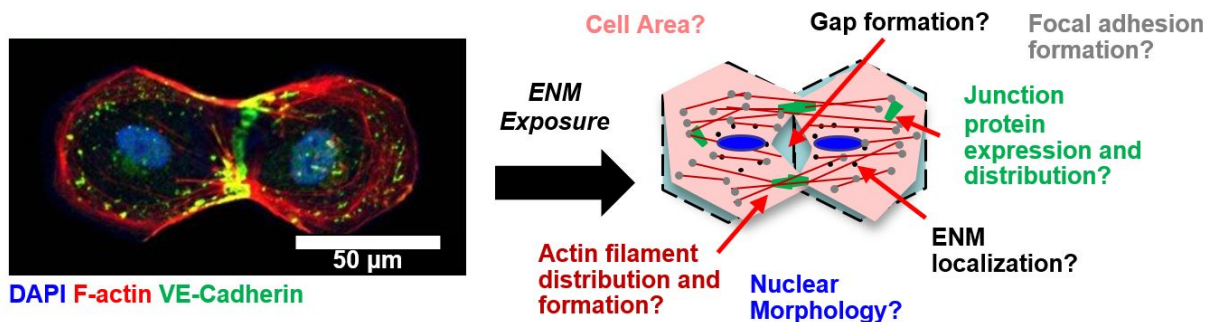
5

6 Feyisayo Eweje,[†] Herdeline Ann M. Ardoña,[†] John F. Zimmerman, Blakely B. O'Connor,
7 Seungkuk Ahn, Thomas Grevesse, Karla N. Rivera, Philip Demokritou and Kevin Kit Parker*

8

9

10



11

12

13 Micropatterned endothelial pairs enable the analysis of the impacts of nanomaterial exposure
14 on cellular-level remodeling processes and vascular barrier integrity.

15

16

17

18

19

20

21